Three-dimensional numerical model for wave-induced seabed response around mono-pile

3-D numerical model for wave-seabed interactions around mono-pile

T.T. Sui[abc], C. Zhang[ab*], Y.K. Guo[c], J.H. Zheng[ab*], D.S. Jeng[d], J.S. Zhang[ab] and W. Zhang[ab]

[a]*State Key Laboratory of Hydrology-Water Resources and Hydraulic Engineering, Hohai University, Nanjing, China.*

[b]*College of Harbour, Coastal and Offshore Engineering, Hohai University, Nanjing, China.*

[c]*School of Engineering, University of Aberdeen, Aberdeen, UK.*

[d]*Griffith School of Engineering, Griffith University Gold Coast Campus, Queensland, Australia.*

***corresponding authors:**

C. Zhang: zhangchi@hhu.edu.cn

J.H. Zheng: jhzheng@hhu.edu.cn

3-D numerical model for wave-seabed interactions around mono-pile

In this study, a new three-dimensional (3-D) model was developed to provide further understanding of the mechanism for wave-seabed interaction around mono-pile. Based on poro-elastic theory, the fully dynamic (FD) formulations were adopted in the present model to simulate pore water pressure, soil stresses, soil and mono-pile displacements. Stress boundary condition was first applied at the seabed-structure interface. Good agreement between numerical simulation and experimental results was obtained. Based on parametric study, numerical results indicated: (1) Non-linear wave diffraction and reflection have significant effects on pore water pressure around mono-pile. (2) The most sensitive position for seabed parameter to pore water pressure around mono-pile locates in front of mono-pile while the least sensitive position is at the position of angle $3\pi/4$ with respect to incident wave direction. (3) The increase of mono-pile horizontal displacement corresponds to the increase of wave height and the decrease of seabed Young's modulus.

Keywords: three-dimensional (3D) model; wave-seabed interaction; wave diffraction; porous seabed; mono-pile; mono-pile displacement.

1. Introduction

Mono-pile foundation has been widely used as the supporter of offshore structures in the past decades, particularly in offshore wind power industry (EWEA 2009). The offshore marine structures usually suffer considerable loadings from ocean waves, currents, wind and earthquakes during their lifetime. These loadings may cause great instability of the seabed around marine structures, which is responsible of most collapses of the structures (Smith and Gordon 1983; Sumer and Fredsoe 2002; Sumer

2014). When the progressive wave encounters a mono-pile, wave reflection and diffraction generate a three-dimensional (3D) field of non-linear wave pressure loading on wave-seabed interface and wave-structure interface. Such non-linear wave pressures are responsible for the dynamic response of seabed and mono-pile, which is closely associated with the instability of the foundation.

The problems of wave induced soil response have been intensively studied by coastal and geotechnical engineers since 1970s. Based on Biot's theory (QS model) (Biot 1941), ignoring both inertial terms of soil and water, analytical solutions for the pore water pressures, effective stress and displacements were proposed (Yamamoto et al. 1978; Madsen 1978; Jeng and Hsu 1996). The effect of the anisotropic and non-homogeneous soil property on the response of seabed to wave actions was analytically investigated (Yamamoto 1981; Hsu and Jeng 1994; Jeng and Seymour 1997; Jeng 1997). Regarding dynamic response, Zienkiewicz et al. (1980) may have been the first to develop one-dimensional (1D) formulations of partly dynamic (PD) and fully dynamic (FD) model. Following their study, the effect of inertia force on wave-induced soil response was investigated using linear and non-linear wave theories (Jeng et al. 1999; Jeng and Cha 2003). Recently, Ulker et al. (2009) further extended the above analytical solutions under plane strain condition using three formulations (QS, PD, FD), and clarified the applicable range of each approximation. Though these analytical approaches demonstrated some features of the soil response to wave actions, they have not considered the effect of the structures under complex conditions in this process.

To investigate the wave-seabed interaction around marine structures, various

numerical models have been developed in the past decades. Based on Navier-Stokes or Boussinesq-type equations, the porous flow inside the permeable structure and seabed was simulated by considering the flow continuity at the interface between porous media and water (Cruz et al. 1997; Shao 2010). In these studies, both seabed and structures were treated as rigid porous media and the stress and strain of the seabed and structure were omitted. The pore pressure and seabed and structure stress were considered in the following studies which is based on Biot's equations (QS model) or its extensions (PD model and FD model). Among these, the potential flow theory (Mostafa et al. 1999; Mizutani et al. 1998; Jeng et al. 2001; Ulker et al. 2010) and Reynolds-averaged Navier-Stokes (RANS) equations (Zhang JS et al. 2011; Zhang et al. 2012; Jeng et al. 2013) were used to provide wave loading and investigate the seabed and structures response in 2D condition. However, the 2D study cannot simulate the wave diffraction that normally occurs around the marine structures. As such, various 3D models were developed. Majority of these 3D investigations focused on seabed response around breakwater in which marine structure stands on the seabed instead of embedded into seabed like mono-pile (Li and Jeng 2008; Jeng and Ou 2010; Ye et al. 2013). Li et al. (2011) conducted a simple simulation using analytical wave theory and QS soil model to investigate seabed response around mono-pile. However, they did not consider the wave reflection and diffraction in their study because of small diameter of the pile foundation compared with the wavelength. More recently, Chang et al. (2014) considered 3D wave diffraction and reflection in their study of wave induced seabed response around high-rising structure foundation. However, the motion of mono-pile

and the effect of wave diffraction on seabed and structure dynamic response were not considered in their study. To the authors' best knowledge, the influences of stress boundary condition at seabed-structure interface on seabed response around cyclic loading applied mono-pile have not been properly investigated (Cuellar 2011; Hansen 2012).

In this study, a new 3D model for wave-seabed interaction around mono-pile was proposed. Pressure boundary condition at the interface between wave-seabed and wave-mono-pile was specified using the open-source FUNWAVE code by solving fully non-linear Boussinesq equation (Wei et al. 1995; Shi et al. 2001; Kirby et al. 2003). The fully non-linear wave reflection and diffraction around mono-pile was considered. Seabed and mono-pile dynamic response were considered by poro-elastic seabed model which is based on FD equations. New numerical technique of material identification technique (MIT), which is used for identifying different domains (e.g. air, wave, seabed and structure) was proposed in this model. Furthermore, the stress boundary condition at the seabed-mono-pile interface was specified in the simulation, which is ignored in most previous studies. The present model was validated using the laboratory experiments. Then, the model was applied to simulate the dynamic response of seabed and mono-pile under non-linear wave action. Parametric studies were carried out to investigate the effects of seabed characteristics (permeability, saturation degree and Young's modulus) and wave characteristics (wave height and wave number) on seabed response around a mono-pile.

2. Numerical Model

2.1. Seabed model

2.1.1. Governing equations

Based on the poro-elastic theory (Zienkiewicz et al. 1980), the governing equations which are the overall equilibrium equation of soil, equilibrium equation of pore fluid flow and mass balance equation of the mixed media can be expressed in tensor form as:

$$\sigma_{ij,j} + \rho g_i = \rho \ddot{u}_i + \rho_f \ddot{w}_i \tag{1}$$

$$-p_{,i} + \rho_f g_i = \rho_f \ddot{u}_i + \frac{\rho_f \ddot{w} i}{n} + \frac{\rho_f g_i}{k_i} \dot{w}_i \tag{2}$$

$$\dot{u}_{i,i} + \dot{w}_{i,i} = -\frac{n}{k_f} \dot{p} \tag{3}$$

where σ_{ij} is the total stress, ρ is the average density of the porous medium, p is the pore water pressure, ρ_f is the density of water, g_i is the gravitational acceleration in the i-direction, u_i is the displacement of soil matrix in the i-direction, w_i is the average relative displacement of the fluid to the solid skeleton in the i-direction, k_i is the permeability of the porous medium in the i-direction, n is the porosity of solid phase, k_f is the bulk modulus of pore water.

In Equations (1)-(3), the soil strain is defined by

$$\varepsilon_{ij} = \frac{u_{i,j} + u_{j,i}}{2} \tag{4}$$

The compressibility of pore fluid is defined as (Yamamoto et al. 1978):

$$\beta = \frac{1}{k_f} + \frac{1 - S_r}{\rho_f g d} \tag{5}$$

where d is the water depth and S_r is the degree of saturation. It is noted that the above definition for compressibility of pore fluid is only valid for high degree of saturation

(Pietruszczak and Pande 1996).

The total stresses are given in terms of the effective stresses and pore pressure (Terzaghi's Principle):

$$\sigma_{ij} = \sigma'_{ij} - \delta_{ij} p \tag{6}$$

where δ_{ij} is the Kronecker delta denotation, σ'_{ij} is the effective stress. Note that above definition implies that tensional stress is positive. A cross-anisotropic material has the same elastic properties in horizontal directions but different in the vertical direction, caused by the format of deposition, particle shape and stress history. For a cross-anisotropic elastic seabed, the following relationships exist (Pickering 1970):

$$\frac{\mu_{vh}}{\mu_{hv}} = \frac{E_h}{E_v} = \Omega \tag{7}$$

$$G_h = \frac{E_h}{2(1+\mu_{hh})} = \frac{\Omega E_v}{2(1+\mu_{hh})} = G E_v \tag{8}$$

$$G_v = \Lambda E_v \tag{9}$$

where μ_{vh}, μ_{hv} and μ_{hh} are the Poisson ratios in different directions, E_h and E_v are Young's modulus in the horizontal direction and in the vertical directions, G_h and G_v are shear modulus in the horizontal and the vertical directions, Ω is a non-dimensional parameter, Λ is the anisotropic constant. Equations (7)-(9) indicate that the cross-anisotropic elastic seabed behaviour can be described by the five parameters, namely E_v, μ_{hh}, μ_{vh}, Ω, and Λ. Note that for an isotropic seabed, $\mu_{hh} = \mu_{vh}$, $\Omega = 1$ and $\Lambda = 1/2(1+\mu_{hh})$.

For the constitutive behaviour of the soil under the plain strain condition, the

poro-elastic stress-strain relationship in an anisotropic seabed can be expressed as:

$$\sigma_x^{'} = E_v\left[C_{11}\frac{\partial u_x}{\partial x} + C_{12}\frac{\partial u_y}{\partial y} + C_{13}\frac{\partial u_z}{\partial z}\right] \tag{10}$$

$$\sigma_y^{'} = E_v\left[C_{12}\frac{\partial u_x}{\partial x} + C_{11}\frac{\partial u_y}{\partial y} + C_{13}\frac{\partial u_z}{\partial z}\right] \tag{11}$$

$$\sigma_z^{'} = E_v\left[C_{13}\frac{\partial u_x}{\partial x} + C_{13}\frac{\partial u_y}{\partial y} + C_{33}\frac{\partial u_z}{\partial z}\right] \tag{12}$$

$$\tau_{xy} = GE_v\left[\frac{\partial u_x}{\partial y} + \frac{\partial u_y}{\partial x}\right] = \tau_{yx} \tag{13}$$

$$\tau_{xz} = \Lambda E_v\left[\frac{\partial u_x}{\partial z} + \frac{\partial u_z}{\partial x}\right] = \tau_{zx} \tag{14}$$

$$\tau_{yz} = \Lambda E_v\left[\frac{\partial u_y}{\partial z} + \frac{\partial u_z}{\partial y}\right] = \tau_{zy} \tag{15}$$

where

$$C_{11} = \Omega\left(1 - \mu_{hv}\mu_{vh}\right)/\Delta \tag{16}$$

$$C_{12} = \Omega\left(\mu_{hv}\mu_{vh} + \mu_{hh}\right)/\Delta \tag{17}$$

$$C_{13} = \Omega\mu_{vh}\left(1 + \mu_{hh}\right)/\Delta \tag{18}$$

$$C_{33} = \left(1 - \mu_{hh}^2\right)/\Delta \tag{19}$$

$$\Delta = \left(1 + \mu_{hh}\right)\left(1 - \mu_{hh} - 2\mu_{hv}\mu_{vh}\right) \tag{20}$$

In natural environments, the seabed is almost always non-homogeneous due to self-gravity consolidation and complex coastal dynamics (Zhang C et al. 2011). In the

present model, all the seabed parameters, such as total porous media density (ρ_s), water density (ρ_w), permeability (k), the porosity of the solid phase (n), the bulk modulus of pore water (k_f), vertical Yong's modulus (E_v), vertical Poisson's ratios (u_{hh}), horizontal Poisson's ratios (u_{vh}), are functions of the spatial locations (x, y, z). Therefore, the model considers the true coastal environmental situation.

Based on the above analysis, the governing equations of fully dynamic seabed model including the effects of fully non-homogeneous and anisotropic seabed can be expressed in scalar form as:

$$\begin{aligned}
&E_v[C_{11}\frac{\partial^2 u_x}{\partial x^2}+G\frac{\partial^2 u_x}{\partial y^2}+\Lambda\frac{\partial^2 u_x}{\partial z^2}+(C_{12}+G)\frac{\partial^2 u_y}{\partial x\partial y}+(C_{13}+\Lambda)\frac{\partial^2 u_z}{\partial x\partial z}\\
&+\frac{\partial C_{11}}{\partial x}\frac{\partial u_x}{\partial x}+\frac{\partial G}{\partial y}\frac{\partial u_x}{\partial y}+\frac{\partial \Lambda}{\partial z}\frac{\partial u_x}{\partial z}+\frac{\partial G}{\partial y}\frac{\partial u_y}{\partial x}+\frac{\partial C_{12}}{\partial x}\frac{\partial u_y}{\partial y}+\frac{\partial C_{13}}{\partial x}\frac{\partial u_z}{\partial z}+\frac{\partial \Lambda}{\partial z}\frac{\partial u_z}{\partial x}]\\
&+\frac{\partial E_v}{\partial x}\left(C_{11}\frac{\partial u_x}{\partial x}+C_{12}\frac{\partial u_y}{\partial y}+C_{13}\frac{\partial u_z}{\partial z}\right)+\frac{\partial E_v}{\partial y}\left(G\frac{\partial u_x}{\partial y}+G\frac{\partial u_y}{\partial x}\right)+\frac{\partial E_v}{\partial z}\left(\Lambda\frac{\partial u_x}{\partial z}+\Lambda\frac{\partial u_z}{\partial x}\right)\\
&-\frac{\partial p}{\partial x}=\rho_f\frac{\partial^2 w_x}{\partial t^2}+\rho\frac{\partial^2 u_x}{\partial t^2}
\end{aligned}\tag{21}$$

$$\begin{aligned}
&E_v[G\frac{\partial^2 u_y}{\partial x^2}+C_{11}\frac{\partial^2 u_y}{\partial y^2}+\Lambda\frac{\partial^2 u_y}{\partial z^2}+(C_{12}+G)\frac{\partial^2 u_x}{\partial x\partial y}+(C_{13}+\Lambda)\frac{\partial^2 u_z}{\partial y\partial z}\\
&+\frac{\partial C_{12}}{\partial y}\frac{\partial u_x}{\partial x}+\frac{\partial G}{\partial x}\frac{\partial u_x}{\partial y}+\frac{\partial G}{\partial x}\frac{\partial u_y}{\partial x}+\frac{\partial C_{11}}{\partial y}\frac{\partial u_y}{\partial y}+\frac{\partial \Lambda}{\partial z}\frac{\partial u_y}{\partial z}+\frac{\partial \Lambda}{\partial z}\frac{\partial u_z}{\partial y}+\frac{\partial C_{13}}{\partial y}\frac{\partial u_z}{\partial z}]\\
&+\frac{\partial E_v}{\partial x}\left(G\frac{\partial u_x}{\partial y}+G\frac{\partial u_y}{\partial x}\right)+\frac{\partial E_v}{\partial y}\left(C_{12}\frac{\partial u_x}{\partial x}+C_{11}\frac{\partial u_y}{\partial y}+C_{13}\frac{\partial u_z}{\partial z}\right)+\frac{\partial E_v}{\partial z}\left(\Lambda\frac{\partial u_y}{\partial z}+\Lambda\frac{\partial u_z}{\partial y}\right)\\
&-\frac{\partial p}{\partial y}=\rho_f\frac{\partial^2 w_y}{\partial t^2}+\rho\frac{\partial^2 u_y}{\partial t^2}
\end{aligned}\tag{22}$$

$$\begin{aligned}
&E_v[\Lambda\frac{\partial^2 u_z}{\partial x^2}+\Lambda\frac{\partial^2 u_z}{\partial y^2}+C_{33}\frac{\partial^2 u_z}{\partial z^2}+(C_{13}+\Lambda)\frac{\partial^2 u_x}{\partial x\partial z}+(C_{13}+\Lambda)\frac{\partial^2 u_y}{\partial y\partial z}\\
&+\frac{\partial C_{13}}{\partial z}\frac{\partial u_x}{\partial x}+\frac{\partial \Lambda}{\partial x}\frac{\partial u_x}{\partial z}+\frac{\partial C_{13}}{\partial z}\frac{\partial u_y}{\partial y}+\frac{\partial \Lambda}{\partial y}\frac{\partial u_y}{\partial z}+\frac{\partial \Lambda}{\partial x}\frac{\partial u_z}{\partial x}+\frac{\partial \Lambda}{\partial y}\frac{\partial u_z}{\partial y}+\frac{\partial C_{33}}{\partial z}\frac{\partial u_z}{\partial z}]\\
&+\frac{\partial E_v}{\partial x}\left(\Lambda\frac{\partial u_x}{\partial z}+\Lambda\frac{\partial u_z}{\partial x}\right)+\frac{\partial E_v}{\partial y}\left(\Lambda\frac{\partial u_y}{\partial z}+\Lambda\frac{\partial u_z}{\partial y}\right)+\frac{\partial E_v}{\partial z}\left(C_{13}\frac{\partial u_x}{\partial x}+C_{13}\frac{\partial u_y}{\partial y}+C_{33}\frac{\partial u_z}{\partial z}\right)\\
&-\frac{\partial p}{\partial z}-\rho g=\rho_f\frac{\partial^2 w_z}{\partial t^2}+\rho\frac{\partial^2 u_z}{\partial t^2}
\end{aligned}\tag{23}$$

$$-\frac{\partial p}{\partial x}=\frac{\rho g}{k_x}\frac{\partial w_x}{\partial t}+\rho_f\frac{\partial^2 u_x}{\partial t^2}+\frac{\rho_f}{n}\frac{\partial^2 w_x}{\partial t^2} \tag{24}$$

$$-\frac{\partial p}{\partial y}=\frac{\rho g}{k_y}\frac{\partial w_y}{\partial t}+\rho_f\frac{\partial^2 u_y}{\partial t^2}+\frac{\rho_f}{n}\frac{\partial^2 w_y}{\partial t^2} \tag{25}$$

$$-\frac{\partial p}{\partial z}+\rho_f g=\frac{\rho g}{k_z}\frac{\partial w_z}{\partial t}+\rho_f\frac{\partial^2 u_z}{\partial t^2}+\frac{\rho_f}{n}\frac{\partial^2 w_z}{\partial t^2} \tag{26}$$

$$\frac{\partial u_x}{\partial x}\frac{\partial u_x}{\partial t}+\frac{\partial u_y}{\partial y}\frac{\partial u_y}{\partial t}+\frac{\partial u_z}{\partial z}\frac{\partial u_z}{\partial t}+\frac{\partial w_x}{\partial x}\frac{\partial w_x}{\partial t}+\frac{\partial w_y}{\partial y}\frac{\partial w_y}{\partial t}+\frac{\partial w_z}{\partial z}\frac{\partial w_z}{\partial t}=-n\beta\frac{\partial p}{\partial t} \tag{27}$$

The above governing equations provide a complete set of formulations for the investigation of the full-dynamic responses of fluid and soil in a non-homogeneous and anisotropic porous seabed. The accelerations due to soil motion and pore fluid are considered. Ignoring the acceleration due to pore fluid or/and soil motion reduces these general formulations to the conventional *u-p* model (PD) or the Biot's consolidation model (QS).

2.1.2. Numerical implementation

General description. The Cartesian coordinate system was adopted in the present model (see Figure 1). The model applies a staggered rectangular grid. The pore pressure and the seabed/structure parameters are defined in cell centers, while the soil/fluid displacements, soil stresses and seepage flow velocities are defined at the cell interfaces, as shown in Figure 1. The second-order Crank-Nicolson type implicit Finite-Difference-Method (FDM) is used to discretize the governing equations in time and space. The Alternating-Direction-Implicit (ADI) method and the Leap-Frog method are used to solve the multi-variables in the differential equations with multi-dimensions. The under-relaxation technique was used by changing the under-relaxation factor during

the simulation in order to speed up the convergence of the calculation (Guo 2014). This was done carefully so that no divergence or undue instability occurred in the simulation.

Material identification technique (MIT). A material identification technique (MIT) was developed to identify the various 3D domains of grid cells occupied by various materials (air, wave, seabed, structure), based on the structured background grid system.

Firstly, we input the 3D domain information of all materials. Each domain is constructed by a number of horizontal polygons and each polygon is constructed by a fixed number of vertices, as shown in Figure 2a. In Figure 2a, m is the number of horizontal polygons which constructs the domain in the vertical direction. The number of vertices n should be constant for all the polygons. x_{ij} and y_{ij} are the horizontal coordinates of the *j-th* vertices of the *i-th* polygon. Since the polygons are horizontal, all vertices of the *k-th* polygon will share one vertical coordinate z_m. A single horizontal polygon is constructed by linking its vertices with straight lines in the order of the list (from vertices 1 to vertices n). A 3D domain is then constructed by linking the polygons with faces in the order of the list (from polygon 1 to polygon m). If the edge of the domain is curvilinear (like circular mono-pile in this study) rather than rectilinear, the numbers of polygons and vertices can be increased to improve the computational accuracy. Taking one simple case (m = 3, n = 5) for instance (see Figure 2b), the three-united polygons can define the range of one material (air, wave, seabed, structure) in 3D space.

Secondly, it is found that the grid cells inside each material domain and define these grid cells with the corresponding material materials. Once all grid cells have been

assigned with certain material parameters, the computational boundaries between different materials can be found. According to different pairs of materials involved at the boundaries, different boundary conditions are applied which will be described in section 2.3. Using MIT, it is convenient to set up complex wave-seabed-structure configurations in the present model.

2.2. Wave model

The FUNWAVE 2.0 (Kirby et al. 2003) model was adopted to calculate wave-induced pressure at wave-seabed boundary and wave-structure boundary, which is the input for the seabed model. The governing equations in FUNWAVE 2.0 are based on the non-linear Boussinesq equations derived by Wei et al. (1995). To have a better fitting of the complex configuration boundary. Discretization of the equations on the staggered grid in generalized curvilinear coordinates was conducted by Shi et al. (2001) In FUNWAVE 2.0, different levels of the Boussinesq approximations can be chosen by setting an equation ID in the input file. For details of the FUNWAVE 2.0, readers are referred to Kirby et al. (2003).

2.3. Boundary conditions

There are five boundary conditions to be specified in this model: lateral and bottom boundary condition of the seabed, wave-seabed boundary condition, seabed-structure boundary condition, wave-structure boundary condition and air-structure boundary condition (see Figure 3).

2.3.1. Lateral and bottom boundary conditions of the seabed

The materials at the lateral and bottom boundaries of the seabed are assumed to be impermeable and rigid. Therefore, the soil displacements and the normal gradient of pore pressures are zero:

$$u_{soil} = 0\,,\quad \frac{\partial p}{\partial n} = 0 \tag{28}$$

2.3.2.Wave-seabed boundary condition

At the seabed surface, the Dirichlet conditions are applied. The wave induced pore pressure is equal to the wave pressure, while the vertical effective stress and shear stresses of soil are equal to the wave stresses:

$$p = p_w\,,\quad \sigma'_{soil} = \sigma_w\,,\quad \tau_{soil} = \tau_w \tag{29}$$

It should be noted here that the stresses of water (σ_w and τ_w) are assumed to zero at the present study.

2.3.3 Seabed-structure boundary condition

At the seabed-structure boundary, assuming the structure is impermeable and rigid, the normal gradient of pore pressures is then zero:

$$\frac{\partial p}{\partial n} = 0 \tag{30}$$

It is further assumed that there is no relative displacement of soil with respect to the structure at the interfaces between soil and structure (known as "no slip" boundary):

$$u_{soil} = u_{structure} \tag{31}$$

Furthermore, the condition of the total stress equilibrium is specified which has not been considered in previous study of wave-seabed-structure interactions:

$$\sigma_{structure} = \sigma'_{soil} - p\,, \quad \tau_{structure} = \tau_{soil} \tag{32}$$

2.3.4. Wave-structure boundary condition

At the wave-structure boundary, the condition of the total stress equilibrium is applied:

$$\sigma_{structure} = \sigma_w - p_w\,, \quad \tau_{structure} = \tau_w \tag{33}$$

2.3.5. Air-structure boundary condition

At the air-structure boundary, it is reasonable to assume that the air-flow effect on the structure is negligible compared to the water waves. Therefore, all stresses are zero at this boundary:

$$\sigma_{structure} = 0\,, \quad \tau_{structure} = 0 \tag{34}$$

2.4. Integrated process

It is noted that the present model is an integrated model, in which the effect of small movement of seabed and structure on wave progression is not considered (the so-called one way coupling). The wave model FUNWAVE 2.0 will generate wave pressure for seabed model. The open source code of Kriging 3D (Deutsch and Journel 1997) in the seabed model was used to capture wave pressure from wave model at the both wave-structure and wave-seabed interfaces. A working procedure of this integrated

model is shown in Figure 4.

3. Model Validation

Since there are no 3D experiments for wave induced seabed response around marine structures, 2D model were performed for the purpose of the model validation against the laboratory experiments (Lu 2005; Tsai and Lee 1995; Tsui and Helfrich 1983). The detailed input soil and wave properties for model validation are listed in Table 1. Though the details of the laboratory experiments can be found in Lu (2005), Tsai and Lee (1995) and Tsui and Helfrich (1983), we provide a brief description of the experiments for completeness and convenience.

3.1. Pore pressure cycling with time

Lu (2005) conducted a serious of laboratory experiments to measure the pore pressure under linear and cnoidal progressive waves in a wave tank, which is 60m long, 1.5m wide and 1.8m high. A number of wave pressure sensors were installed in the soil at different elevation of 20cm, 15 cm, 10 cm and 5 cm from the soil bottom. Linear and cnoidal waves were tested for both the fine and coarse soils. Only the experiments with coarse soil were used for validation of the model. Figure 5 is the comparison of the simulated and measured variation of the wave induced dynamic pore pressure with time for linear wave (figures in the left column) and cnoidal wave (figures in the right column). Both the simulation and measurements show that the dynamic pore pressure induced by linear wave has a regular and relatively flat sinuous format, while irregular thin dynamic pore pressure is generated by cnoidal waves. Figure 5 demonstrates that

the dynamic pore pressure induced by linear wave is smaller than that induced by cnoidal wave. Figure 5 also reveals that the dynamic pore pressure increases with the distance from the soil bottom for both linear and cnoidal waves. This is because the pore water velocity increases with the distance from the soil bottom.

The second validation case is the experiment conducted by Tsai and Lee (1995) who measured the soil response under the standing wave system. Nine pore pressure sensors were installed in the soil to measure the time series of the water pressure, in which five sensors were installed on the left-side of soil at different depths while the other four were located on the line-parallel to the soil surface with the elevation of 40 cm from the soil bottom. The space between two sensors is 10 cm. Figure 6 is the simulated standing wave induced dynamic pore pressure compared with the measurements taken at the various depths on the left-side (figures in left column) and on the line-parallel to the soil surface (figures in right column). The similar scenario (to Figure 5) of the variation of the pore dynamic pressure is found in Figure 6. In general, the simulated dynamic pore pressure agrees well with the measurements, as shown in Figure 5 and Figure 6, indicating that the model proposed can accurately simulate the soil response to waves.

3.2. Vertical distribution of pore water pressure

The third validation case is to examine the vertical distribution of pore water pressure. To this end, Tsui and Helfrich (1983) experiment was used. Tsui and Helfrich (1983) conducted a series of experiments to measure vertical distribution of wave-induced pore pressure in the soil. Loose and dense soils with different permeability and saturation

degrees were tested for a range of wave parameters. Figure 7 shows the comparison of the simulated and measured maximum pore water pressure distribution in which p_{max} is the maximum pressure in soil and p_0 is the maximum pressure at the soil surface within one wave period. The analytical solution of Jeng (2010) was also plotted in Figure 7 for comparison. It is seen that the pore water pressure has a sharp decrease over the upper half depth of soil, followed by a gradual attenuation. The simulation and measurements also demonstrate that the relative pore water pressure within the dense soil is smaller than that in loose soil. This is mainly because the pore water velocity in dense soil is smaller than that in loose soil.

4. Model Application

In the real word, the phenomenon of wave reflection and diffraction exists if the propagation of wave is impeded by offshore structures (Zheng et al. 2011), such as mono-pile. In this study, the present 3D model is applied to investigate the response of seabed and mono-pile under non-linear wave action. The problem under investigation is shown in Figure 8. Parameters of wave, seabed and mono-pile in this study are listed in Table 2, while Table 3 lists the reference parameters used for normalization. Figure 9 provides further details of model setup.

4.1. Consolidation process

Generally speaking, seabed experiences long-time consolidation caused by static water pressure loading and its own gravity. However, the installation of mono-pile can significantly change the seabed conditions around the foundation. Recently, Jeng et al.

(2013) and Ye et al. (2014) considered the consolidation process for the problem of wave-seabed-structure interactions. In this study, we first considered the consolidation under pure static water loading. Then, we installed a mono-pile and investigate the consolidation process under the combination of mono-pile weight and static water loading.

Figure 10 illustrates the final consolidation condition of seabed and mono-pile. The plot of Figure 10a reveals that the pore water pressure is zero within the mono-pile because impermeable boundary condition is implied at seabed-mono-pile interface and water-mono-pile interface. In addition, pore water pressure right beneath the mono-pile is larger than that in the lateral sides. Figure 10b are the soil and mono-pile vertical stress σ'_z. It is seen that σ'_z below the mono-pile is increased because of mono-pile installation. Figure 10b also shows that the vertical stress σ'_z slightly decreases at the seabed-mono-pile interface. This may be caused by no-slip boundary condition specified there. Figure 10c shows the displacements of seabed and mono-pile, which demonstrates that the significant soil displacement takes place near and under the mono-pile caused by the gravity of the mono-pile.

4.2. Seabed response around mono-pile

The integrated model was applied to simulate wave induced dynamic response of seabed and mono-pile in 3D. Such dynamic response is triggered by dynamic wave pressure at the wave-seabed interface and wave-structure interface, and is determined as the difference between full response and initial static consolidation conditions. The variations of pore water pressure and effective stresses due to wave-seabed interaction

were investigated. In addition, the seepage force, which is equal to pore water pressure gradient ($j_x=\partial p/\partial x$, $j_y=\partial p/\partial y$, $j_z=\partial p/\partial z$), was also considered in the simulation. When the seepage force is upward, pore water is forced to move upward, thus the soil is easier to be liquefied. On the contrary, when the seepage force is downward, the soil will be hard to be liquefied. Therefore, the seepage force is an useful indicator to examine the likelihood of liquefaction occurrence.

Figure 11a is the pore water pressure distribution around mono-pile in x-y plane at z = -0.31 and t = 2.95T when the wave trough just arrives at the head of mono-pile. Negative pore water pressure with larger value is found at the front and both sides of mono-pile. Figure 11 (b)-(d) show the distribution of pore water pressure (colour) and seepage force (arrows), σ'_z and σ'_x of soil and mono-pile in the x-z plane (y = 0), respectively. Figure 11b shows that a sharp attenuation of pore water pressure is seen to take place in vertical direction, indicating the large vertical seepage force appears. Larger upward seepage force is also seen to appear in front of mono-pile, indicating that seabed in this region is prone to be liquefied. Figure 11c reveals that a positive-negative-positive-negative pattern (coinciding with wave period) of σ'_z appears, starting from the immediate front of mono-pile. It is also noted that within the front part of mono-pile σ'_z has positive value in upper, negative value in middle and positive value in lower part of mono-pile. This may be ascribed to the fact that the large wave dynamic pressure generates large tension within mono-pile. The region with negative σ'_z (within mono-pile) is compressed by its adjacent higher tension regions. Similar horizontal stress σ'_x distribution around mono-pile takes place though its value is much smaller

than the vertical stress σ'_z. The distribution of the horizontal stress σ'_x demonstrates that the displacement of mono-pile mainly appears in front of mono-pile for the current conditions. The slight displacement compresses soil at the front of mono-pile (point A) while soil is tensioned at later time when wave crest reaches the front of mono-pile (see Figure 12d).

Figure 12 demonstrates the soil and structure dynamic response at time $t = 3.45T$ when wave crest reaches the front of mono-pile. Similar phenomenon to Figure 11 observed except that the sign of various quantities is opposite. At this moment, seepage force in front of mono-pile is downward.

4.3. Pore water pressure profiles at various positions

Pore water pressure attenuation and distribution in the vertical direction is significant to seabed instability. Pore water pressure is generated at the seabed surface and then transmits downwards into seabed. In wave-seabed-mono-pile system, a 3D field of non-linear dynamic wave pressure is generated which greatly affects pore water pressure profiles around the mono-pile.

We investigated the pore water pressure along the circular direction around the mono-pile (Figure 13a). Various positions along the circles can be described by two parameters. They are the local distance (S) from the mono-pile boundary and through the centre of mono-pile, and the local angle α which varies from 0 (at the front of mono-pile) to π (back of mono-pile). Since the results are symmetrical with y-axis, only half of the computational domain is shown in Figure 13a. Figure 13 (b)-(d) present the vertical distribution of pore water pressure at a number of selected positions. Similar

trend is found that a sharp decrease of pore water pressure takes place in upper seabed layer (e.g. from seabed surface to about z = -1.0) followed by a gradual change in lower seabed layer. The pore water pressure reduces to zero at about z = -1.8, indicating that the wave influence is minimal at deep seabed. Figure 13 (b)-(d) also demonstrate that in general pore water pressure is larger when the distance S from the mono-pile boundary is smaller, particularly in front of mono-pile, i.e. small α. This is caused perhaps by the wave-mono-pile interaction induced standing wave in front of mono-pile, which makes different wave pressure for different local distance S. For the same distance S (e.g. along a circle around mono-pile), the effect of angle α on the pore water pressure is complex and mixed due to the complex wave diffraction and reflection around mono-pile and the associated dynamic pressure loading at the seabed surface.

Figure 14 shows the effect of seabed permeability (k) on pore pressure around mono-pile. As presented in Figure 14, larger value of seabed permeability will result in larger value of pore pressure around mono-pile. In addition, the largest difference of pore water pressure for different soil permeabilities k exits in front of mono-pile (α = 0), while the smallest difference is at the position of about $\alpha = 3\pi/4$.

Figure 15 illustrates the effect of seabed saturation (S_r) on pore water pressure around mono-pile. Similar phenomenon to Figure 14, we can find that the increase of pore water pressure corresponds to the increase of seabed saturation. In addition, the smallest difference of pore water pressure for seabed saturation can also be found at the position of about $\alpha = 3\pi/4$, indicating that this position ($\alpha = 3\pi/4$) is the least sensitive position for seabed parameters. Another conclusion can be made that the position in

front of mono-pile ($\alpha = 0$) is the most sensitive position as the largest difference of pore water pressure exists there.

4.4. Effect of wave number on pore water pressure around mono-pile

It is well known that wave diffraction and reflection have close relationships with wave number. Figure 16 shows the effect of wave numbers on the maximum pore water pressure (within one wave period) distribution around mono-pile at z = -0.4 and S = 0.4. Three iso-pressure dashed lines are plotted in Figure 16 for the indication of pore water pressure values. It is seen that the pore water pressure is larger at the front of mono-pile than that at the rear for relatively large wave number, indicating that the presence of mono-pile impedes part of wave power to the front while soil at the back is protected from the direct wave action. Pore water pressure increases with the decrease of wave number K due to the increase of wave power at the seabed surface. It is also noted that as the wave number decreases, pore water pressure distribution becomes more uniform around the mono-pile. It may be concluded that the effect of wave diffraction and reflection is insignificant for sufficiently small wave numbers (i.e. large wave lengths) for the parameter range investigated in this study.

4.5. Displacement of the mono-pile

The periodic wave loading may induce slight periodic rocking of mono-pile. However, this phenomenon was usually ignored in previous studies as most studies on wave-mono-pile interaction assumed that no horizontal mono-pile displacement happens at the boundary of seabed-mono-pile (Li 2012) or only considered the

concerned soil displacement by modifying soil stiffness modulus with empirical formulation (Achmus 2009). The potentially important role of mono-pile displacement in the wave-seabed-mono-pile system was not investigated. In this study, the effect of wave height and seabed Yong's modulus on the horizontal displacement of mono-pile was investigated using the proposed model.

Figure 17 shows the effect of wave height (H) on horizontal displacement of mono-pile, in which dashed lines denote the top and bottom of the mono-pile. It is found that the horizontal maximum displacement of mono-pile (within one wave period) increases with the increase of wave height. It is understandable that larger displacement takes place at the top part of mono-pile under the direct wave action. The displacement of mono-pile sharply decreases below seabed surface where the pore water velocity/pressure is relatively small.

Figure 18 illustrates the effect of seabed Young's modulus (E_s) on horizontal displacement of mono-pile. From Figure 18, we can find that the increase of seabed Young's modulus makes the decrease of mono-pile horizontal displacement, which is reasonable due to the fact that seabed is more rigid with the larger Young's modulus. In the cases simulated in this study (Figures 17-18), the maximum displacement of mono-pile is less than 4×10^{-6} times of mono-pile's radius, which is considered insignificant for wave propagation and this validates the one-way model coupling assumption at wave-seabed and wave-mono-pile interfaces.

5. Conclusions

In this study, a new 3D poro-elastic integrated model based on fully dynamic equations was proposed to investigate the wave-seabed interaction around mono-pile. Stress boundary condition was first specified at the seabed-structure interface. A new numerical technique of material identification technique (MIT) was proposed for identifying different domains in wave-seabed-structure system. The model was validated using several laboratory experiments. Good agreement was obtained between numerical simulation and experimental measurements. The validated model was applied to simulate the dynamic seabed response to wave actions around mono-pile for a range of parameters. The following conclusions can be drawn from this study:

(1). The installation of mono-pile and its induced wave reflection and diffraction significantly affect the distribution of pore water pressure. The pore water pressure is increased at the front and lateral sides of mono-pile while it is decreased at the back. The soil in front of mono-pile is prone to be liquefied.

(2). The vertical stress σ'_z within the front part of mono-pile has a positive-negative-positive (under wave trough) or negative-positive-negative (under wave crest) pattern. Large horizontal stress σ'_x of mono-pile exists at the upper part of mono-pile.

(3). The pore water pressure profiles vary with angle α and distance S defined in Figure 13a. Pore water pressure around mono-pile increases as the saturation degree and permeability of soil increases. The most and least sensitive positions with respect to various seabed parameters are at the position of $\alpha = 0$ (in front of mono-pile) and $\alpha = 3\pi/4$, respectively.

(4). The effect of wave reflection and diffraction on the pore water pressure in the vicinity of mono-pile decreases with the decrease of wave number. For sufficiently small wave numbers, the effect of reflection and diffraction can be negligible.

(5). The horizontal displacement of mono-pile takes place under wave action, which increases as wave height increases and seabed Young's modulus decreases.

Acknowledgements

The work is financially supported by the National Science Fund for Distinguished Young Scholars, the National Natural Science Foundation of China (51209082, 51379071), the Specialized Research Fund for the Doctoral Program of Higher Education of China (20120094120006, 20130094110014), the 111 project (B12032), the program of Sina-UK Education Research Partnership for PhD studies, Jiangsu Graduate Research and Innovation Plan Grant (#CXLX11_0450) and University of Aberdeen.

References

Achmus M, Kuo YS, Abdel-Rahman K. 2009. Behavior of mono-pile foundations under cyclic lateral load. Computers and Geotechnics 36 (5): 725-735.

Biot, MA. 1941. General theory of three-dimensional consolidation. Journal of Applied Physics 26 (2): 155-164.

Chang KT, Jeng DS. 2014. Numerical study for wave-induced seabed response around offshore wind turbine foundation in Donghai offshore wind farm, Shanghai, China. Ocean Engineering 85: 32-43.

Cruz EC, Isobe M, Watanabe A. 1997. Boussinesq equations for wave transformation on porous beds. Coastal Engineering 30 (1-2): 125-156.

Cuellar P. 2011. Pile foundations for offshore wind turbines: numerical and experimental investigations on the behaviour under short-term and long-term cyclic loading [thesis]. Berlin (German): Technical University of Berlin.

Deutsch CV, Journel AG. 1997. GSLIB: Geostatistical Software Library and User's Guide. New York: Oxford University Press.

EWEA. 2009. Oceans of opportunity. Technical report, European wind Energy Association.

Guo YK. 2014. Numerical simulation of the spreading of aerated and nonaerated turbulent water jet in a tank of finite water depth. Journal of Hydraulic Engineering (ASCE), 140(8): 10.1061/(ASCE)HY.1943-7900.0000903.

Hansen NM. 2012. Interaction between seabed soil and offshore wind turbine foundations [thesis]. Lyngby (Denmark): Technical University of Denmark.

Hsu JRC, Jeng DS. 1994. Wave-induced soil response in an unsaturated anisotropic seabed of finite thickness. International Journal for Numerical and Analytical Methods in Geomechanics 18 (11): 785-807.

Jeng DS, Hsu JRC. 1996. Wave-induced soil response in a nearly saturated sea-bed of finite thickness. Geotechnique 46 (3): 427-440.

Jeng DS. 1997. Soil response in cross-anisotropic seabed due to standing waves. Journal of Geotechnical and Geoenvironmental Engineering 123 (1): 9-19.

Jeng DS, Seymour BR. 1997. Response in Seabed of Finite Depth with Variable Permeability. Journal of Geotechnical and Geoenvironmental Engineering 123 (10): 902-911.

Jeng DS, Rahman MS, Lee TL. 1999. Effects of inertia forces on wave-induced seabed response. International Journal of Offshore and Polar Engineering 9(4): 307-313.

Jeng DS, Cha DH, Lin YS, Hu PS. 2001. Wave-induced pore pressure around a composite breakwater. Ocean Engineering 28 (10): 1413-1435.

Jeng DS, Cha DH. 2003. Effects of dynamic soil behavior and wave non-linearity on the wave-induced pore pressure and effective stresses in porous seabed. Ocean Engineering 30 (16): 2065-2089

Jeng DS, Ou J. 2010. 3D models for wave-induced pore pressures near breakwater heads. Acta Mechanica 215 (1-4): 85-104.

Jeng DS. 2010. Porous models for wave-seabed interaction. Berlin: Springer.

Jeng DS, Ye JH, Zhang JS, Liu PLF. 2013. An integrated model for the wave-induced

response around marine structures: Model verifications and applications. Coastal Engineering 72: 1-19.

Kirby JT, Wen L, Shi F. 2003. FUNWAVE 2.0 fully nonlinear boussinesq wave model on curvilinear coordinates. Newark (US): University of Delaware. Research Report CACR-03-xx.

Li J, Jeng DS. 2008. Response of a porous seabed around breakwater heads. Ocean Engineering 35 (8-9): 864-886.

Li M. 2012. Three-dimensional wave-structure interaction modeling using the scaled boundary finite element method [thesis]. Griffith (Australia): Griffith University.

Li XJ, Gao FP, Yang B, Zang J. 2011. Wave-induced pore pressure responses and soil liquefaction around pile foundation. International Journal of Offshore and Polar Engineering 21(3): 233-239.

Lu HB. 2005. The research on pore pressure response to waves in sandy seabed [thesis]. Changsha (China): Changsha University of Science & Technology.

Madsen OS. 1978. Wave-induced pore pressures and effective stresses in a porous bed. Geotechnique 28 (4): 377-393.

Mizutani N, Mostarfa A, Iwata K. 1998. Nonlinear wave, submerged breakwater and seabed dynamic interaction. Coastal Engineering 21 (4): 361-379.

Mostafa A, Mizutani N, Iwata K. 1999. Nonlinear wave, composite breakwater, and seabed dynamic interaction. Journal of Waterway, Port, Coastal and Ocean Engineering 25 (2): 88-97.

Pickering DJ. 1970. Anisotropic elastic parameters for soil. Geotechnique 20 (3): 271-276.

Pietruszczak S, Pande GN. 1996. Constitutive relations for partially saturated soils containing gas inclusions. Journal of Geotechnical Engineering. Journal of Geotechnical Engineering 122 (1): 50-59.

Shao SD. 2010. Incompressible SPH flow model for wave interactions with porous media. Coastal Engineering 57 (3): 304-316.

Shi FY, Dalrymple RA, Kirby JT, Chen Q, Kennedy A. 2001. A fully nonlinear Boussinesq model in generalized curvilinear coordinates. Coastal Engineering 42

(4): 337-358.

Smith AWS, Gordon AD. 1983. Large breakwater toe failures. Journal of Waterway, Port, Coastal, and Ocean Engineering. 109 (2): 253–255.

Sumer BM, Fredsoe J. 2002. The mechanics of scour in the marine environment. Singapore: World Scientific.

Sumer BM. 2014. Liquefaction around marine structures. Singapore: World Scientific.

Tsai CP, Lee TL. 1995. Standing wave induced pore pressure in a porous seabed. Ocean Engineering 22 (6): 505-517.

Tsui Y, Helfrich SC. 1983. Wave-induced pore pressure in submerged sand layer. Journal of Geotechnical Engineering, ASCE 109 (4): 603-618.

Ulker MBC, Rahman MS, Jeng DS. 2009. Wave induced response of seabed: various formulation and their applicability. Applied Ocean Research 31 (1): 12-24.

Ulker MBC, Rahman MS, Guddati MN. 2010. Wave induced dynamic response and instability of seabed around caisson breakwater. Ocean Engineering 37 (17-18): 1522-1545.

Wei G., Kirby JT, Grilli ST, Subramanya R. 1995. A fully nonlinear Boussinesq model for surface-waves.1. highly nonlinear unsteady waves. Journal of Fluid Mechanics 294: 71-92.

Yamamoto T, Koning HL, Sellmeijer H, Hijum EV. 1978. On the response of a poro-elastic bed to water waves. Journal of Fluid Mechanics 87 (1): 193-206.

Yamamoto T. 1981. Wave-induced pore pressures and effective sresses in inhomogeneous seabed foundations. Ocean Engineering 8 (1): 1-16.

Ye JH, Jeng DS, Wang R, Zhu CQ. 2013. A 3-D semi-coupled numerical model for fluid-structures-seabed-interaction (FSSI-CAS 3D): Model and verification. Journal of Fluid and Structures 40: 148-162.

Ye JH, Jeng DS, Liu PLF, Chan AHC, Wang R, Zhu CQ. 2014. Breaking wave-induced response of composite breakwater and liquefaction in seabed foundation. Coastal Engineering 85: 72-86.

Zienkiewicz OC, Chang CT, Bettess P. 1980. Drained, undrained, consolidating and dynamic behaviour assumptions in soils. Geotechnique 30 (4): 385-395.

Zhang C, Zheng JH, Wang YG, Demirbilek Z. 2011. Modeling wave-current bottom boundary layers beneath shoaling and breaking waves. Geo-Marine letters 31 (3): 189-201.

Zhang JS, Jeng DS, Liu FLF. 2011. Numerical study for waves propagating over a porous seabed around a submerged breakwater: PORO-WSSI II model. Ocean Engineering 38 (7): 954-966.

Zhang JS, Jeng DS, Liu PLF, Zhang C, Zhang Y. 2012. Response of a porous seabed to water waves over permeable submerged breakwaters with bragg reglection. Ocean Engineering 43: 1-12.

Zheng JH, Nguyen VT, Zhang C. 2011. Spectral wave transformation model for simulating refraction - diffraction with strongly reflecting coastal structures. Acta Oceanologica Sinica 30 (2): 25-32.

Table captions

Table 1. Wave and soil parameters for model validation.

Experiments & Field measurements	Wave parameters			Soil parameters					
	H(cm)	d(m)	T(s)	ρ_s(kg/m^3)	E_s(N/m^2)	μ_s	k (m/s)	n	S_r
Lu's (2005) experiment	12/14	0.5/0.3	1.2/1.4	2.65×10^{3}	1.4×10^{7}	0.33	1.4×10^{-3}	0.39	0.98
Tsai and Lee (1995) experiment	5.1	0.45	1.5	2.65×10^{3}	6.86×10^{7}	0.3	1.2×10^{-4}	0.38	0.98
Tsui and Helfrich (1983) experiment	2.0	0.488	1.5	2.65×10^{3}	1.33×10^{7}	0.33	$5\times10^{-4}/1\times10^{-3}$	0.3	0.985/0.988

Table2. Physical parameters of monopile, wave and seabed for simulation.

Parameters		Notations	Magnitudes	Units
Pile parameters	Pile radius	R	2.5	m
	Pile length	L	14	m
	Pile density	ρ_p	2650	Kg/m^3
	Young's modulus	E_p	1.0	Gpa
	Possion's ratio	μ_p	0.25	-
Wave parameters	Water depth	d	4	m
	Incident wave angle	β	0	rad
	Wave Period	T	4~20	s
	Water density	ρ_f	1000	Kg/m^3
	Wave amplitude	H	0.2~0.4	m
Seabed parameters	Soil permeability	k	10^{-4}~10^{-3}	m/s
	Soil porosity	n	0.3	-
	Soil density	ρ_s	2650	Kg/m^3
	Soil saturation	S_r	0.980~0.992	-
	Possion's ratio	μ_s	0.33	-
	Young's modulus	E_s	0.05~0.1	Gpa

Table 3. Parameters for model normalization in this study.

Reference parameters	descriptions	Magnitudes	Dimensions
R	Radius of monopile	2.5 m	L
$\rho_f g d$	Static water pressure at seabed surface	39240 pa	N/m^2

Figure captions

pressure at $t = 3.45T$ ($T = 4$s, $H = 0.08$, $k = 1\times10^{-3}$ m/s, $S_r = 0.992$, $E_s = 5\times10^{7}$ N/m^2). (a) Pore water pressure p at x-y plane ($z = -0.31$). (b) Pore water pressure p at x-z plane ($y = 0$). (c) Vertical stress σ'_z at x-z plane ($y = 0$). (d) Horizontal stress σ'_x at x-z plane ($y = 0$).

Figure 13. Pore water pressure distribution at various positions as defined by angle α and distance S ($T = 4$s, $H = 0.08$, $k = 1\times10^{-3}$ m/s, $S_r = 0.992$, $E_s = 5\times10^{7}$ N/m^2). (a) The sketch for simulation. (b) $S = 0.71$. (c) $S = 1.31$. (d) $S = 2.31$.

Figure 14. The effect of soil permeability on pore water pressure distribution around mono-pile (T=4s, $H = 0.08$, $S_r = 0.992$, $E_s = 5\times10^{7}$ N/m^2, $z = -0.31$, $S = 0.71$).

Figure 15. The effect of soil saturation degree on pore water pressure distribution around mono-pile ($T = 4$s, $H = 0.08$, $k = 1\times10^{-3}$ m/s, $E_s = 5\times10^{7}$ N/m^2, $z = -0.31$, $S = 0.71$).

Figure 16. The effect of wave number on pore water pressure distribution around mono-pile ($H = 0.08$, $k = 1\times10^{-3}$ m/s, $S_r = 0.992$, $E_s = 5\times10^{7}$ N/m^2, $z = -0.4$, $S = 0.4$).

Figure 17. The effect of wave height on mono-pile horizontal displacement ($T = 4$s, $k = 1\times10^{-3}$ m/s, $S_r = 0.992$, $E_s = 5\times10^{7}$ N/m^2).

Figure 18. The effect of seabed Young's modulus on mono-pile horizontal displacement ($T = 4$s, $H = 0.08$, $k = 1\times10^{-3}$ m/s, $S_r = 0.992$).

Figure 1
Click here to download high resolution image

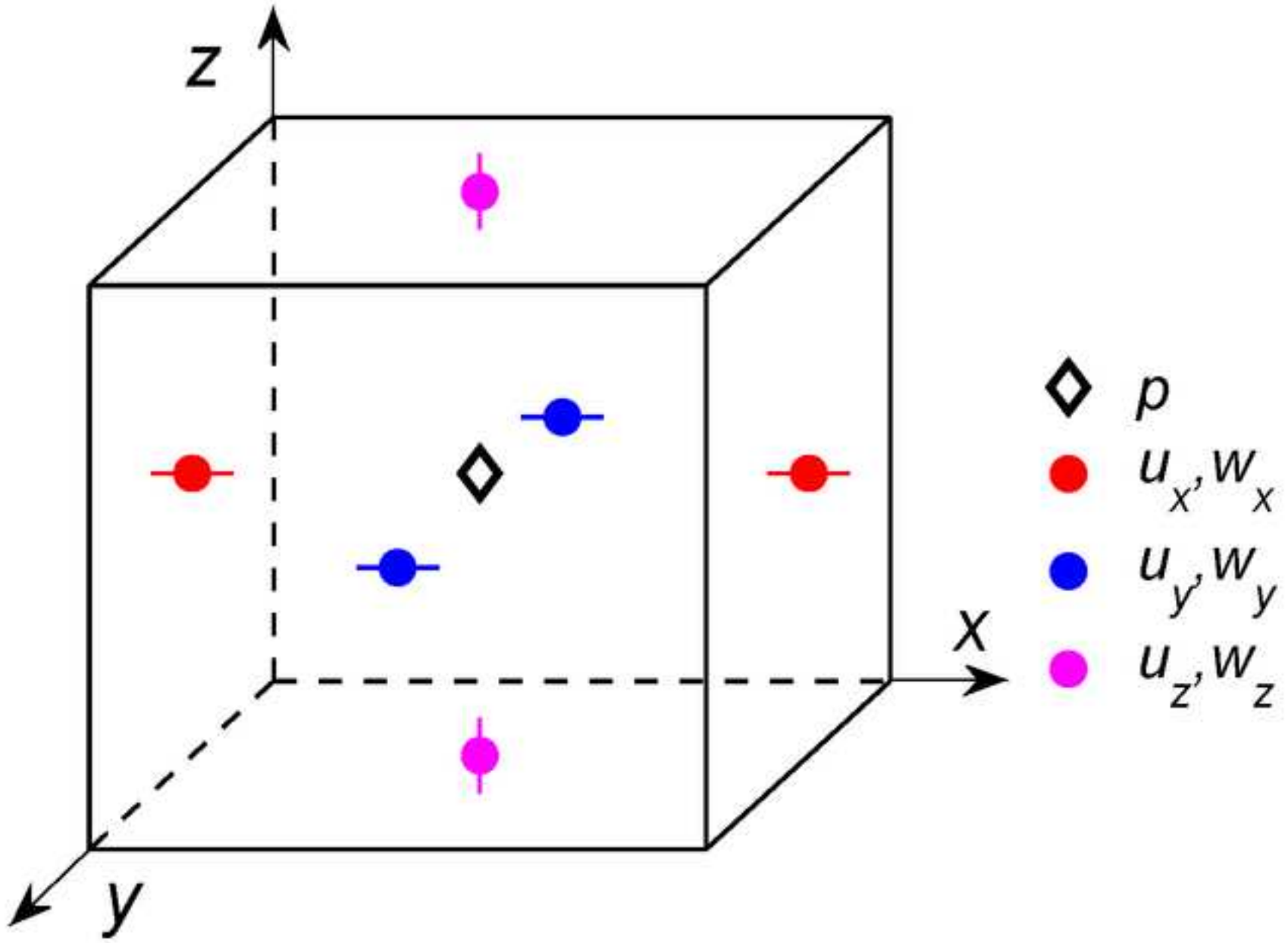

Figure 2
Click here to download high resolution image

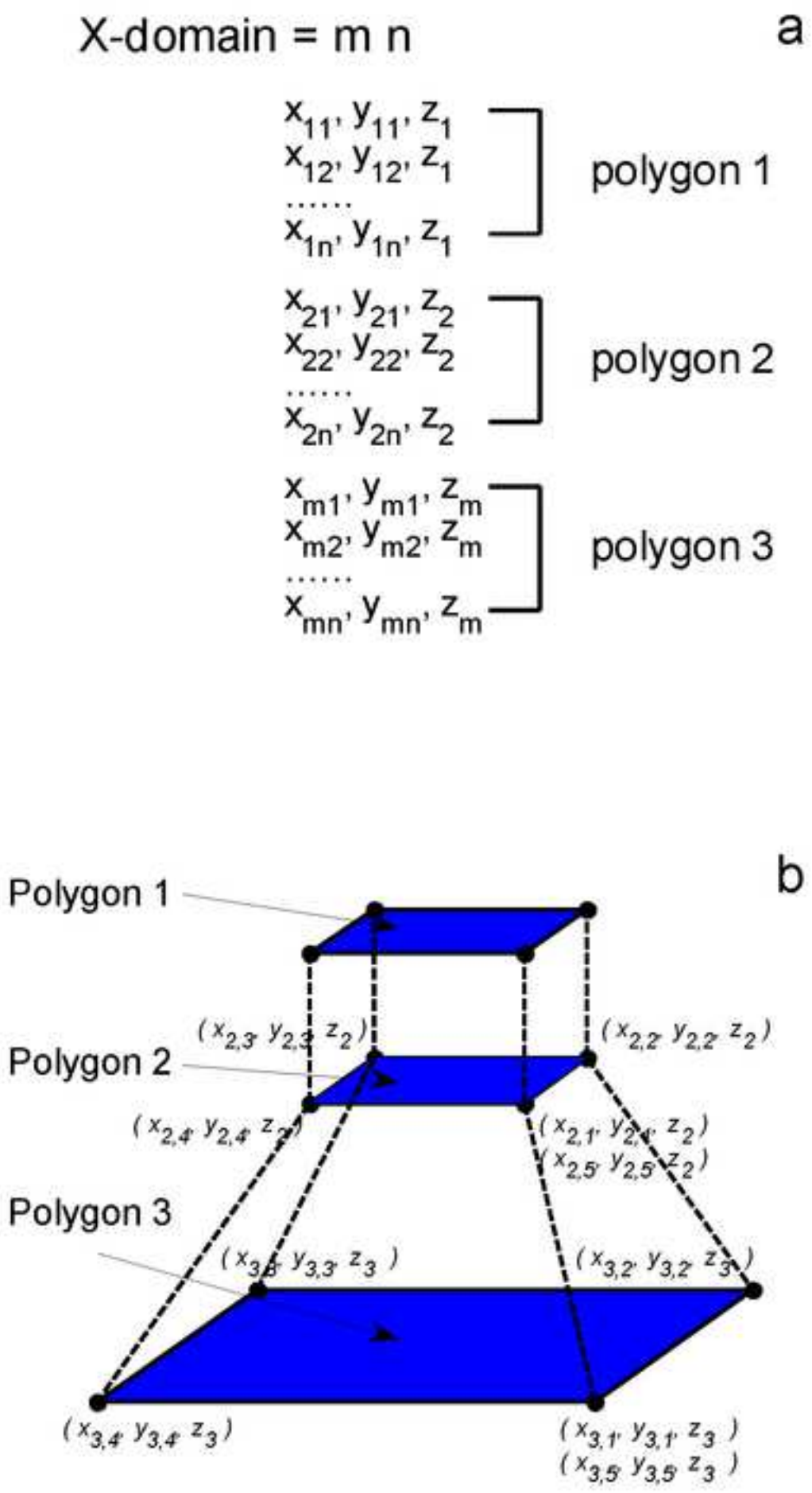

Figure 3
Click here to download high resolution image

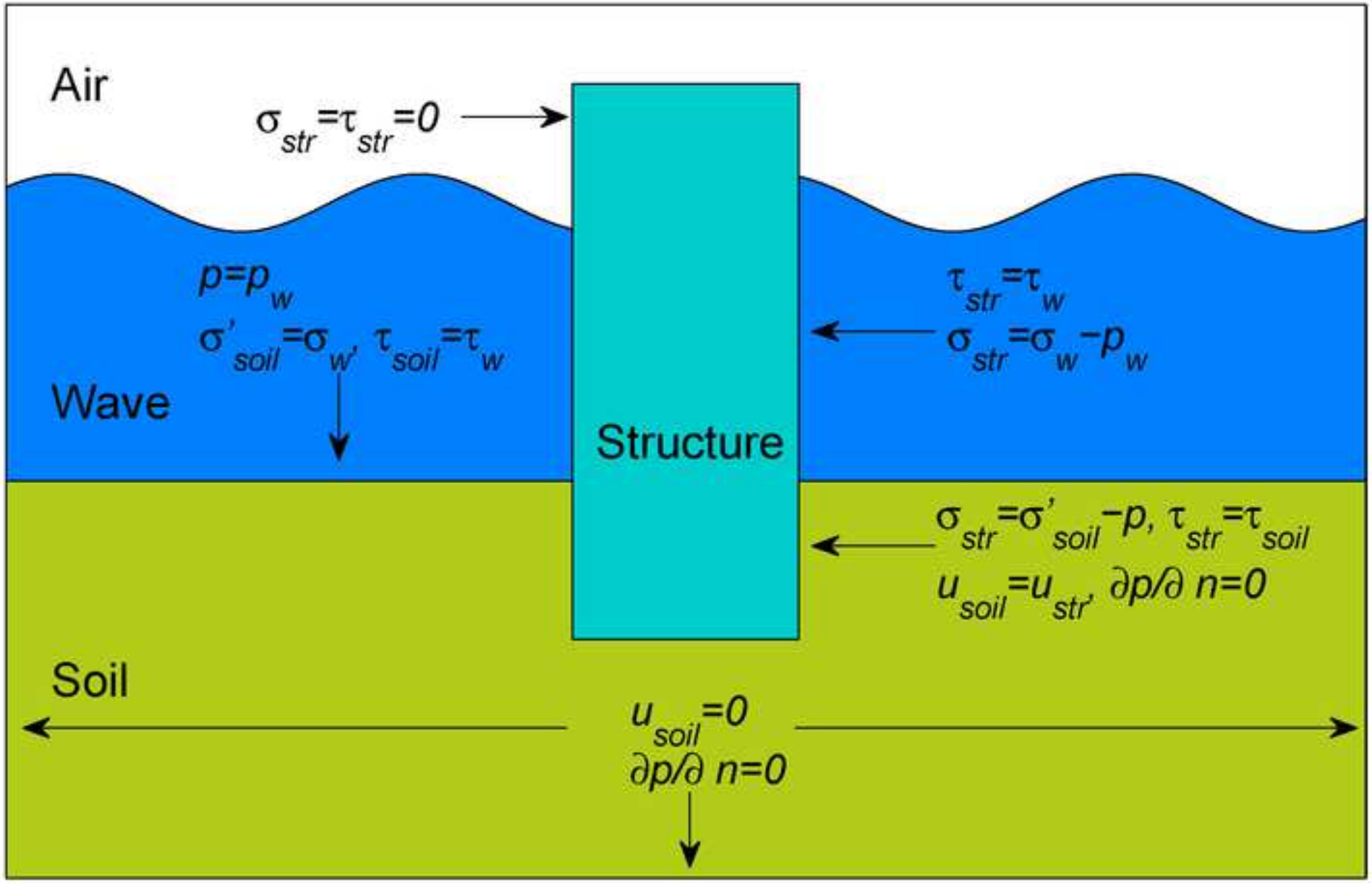

Figure 4
Click here to download high resolution image

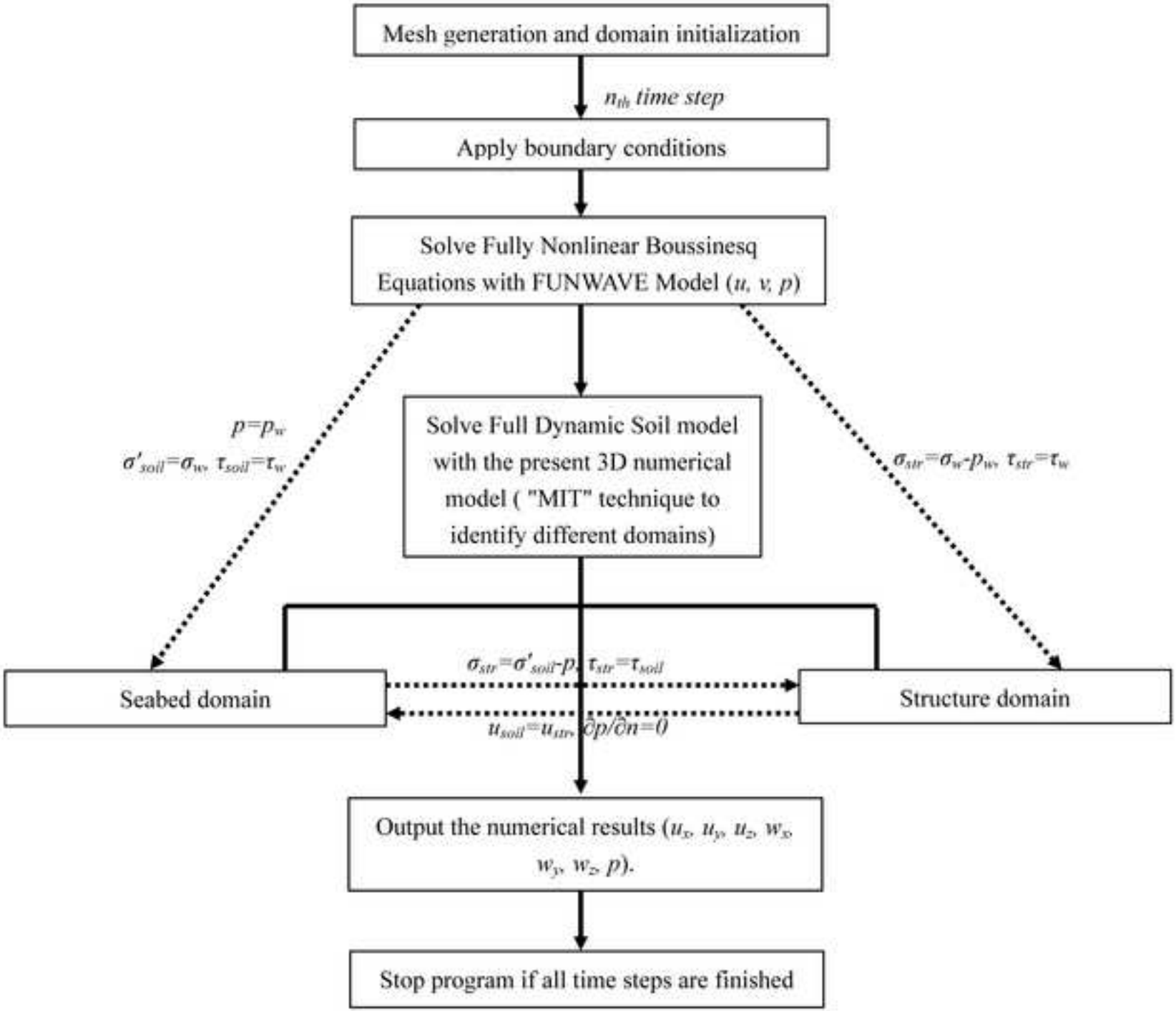

Figure 5
Click here to download high resolution image

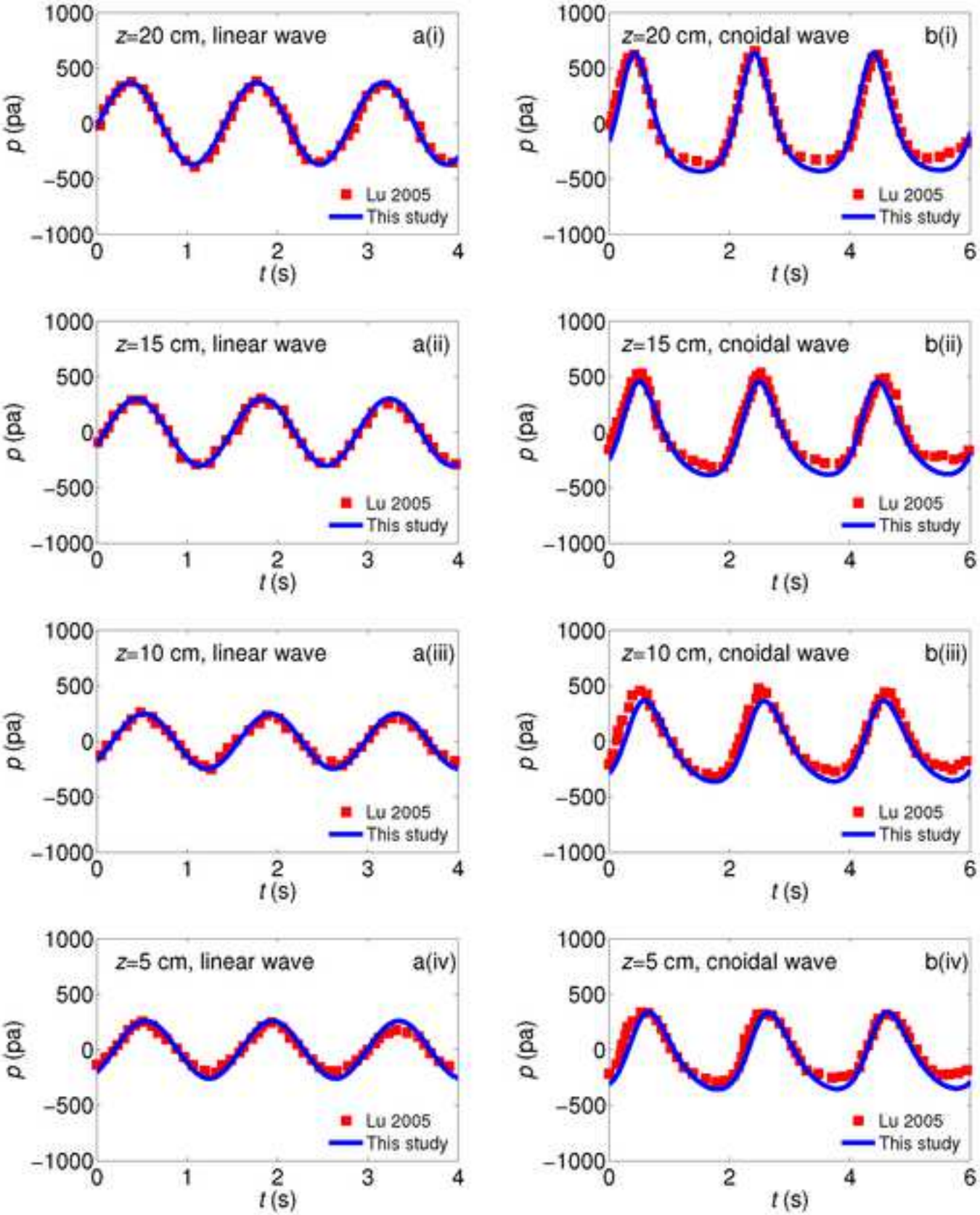

Figure 6
Click here to download high resolution image

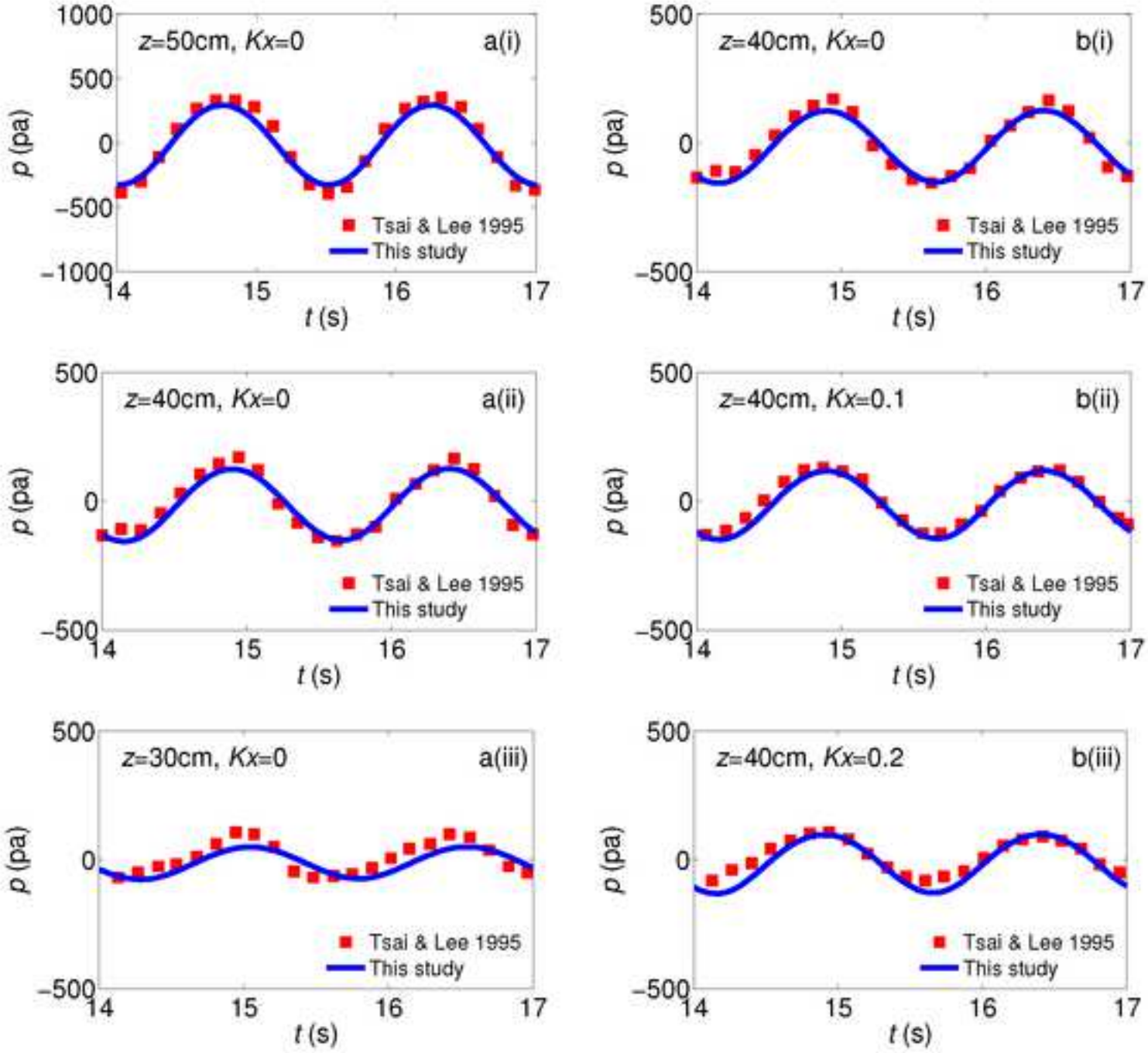

Figure 7
Click here to download high resolution image

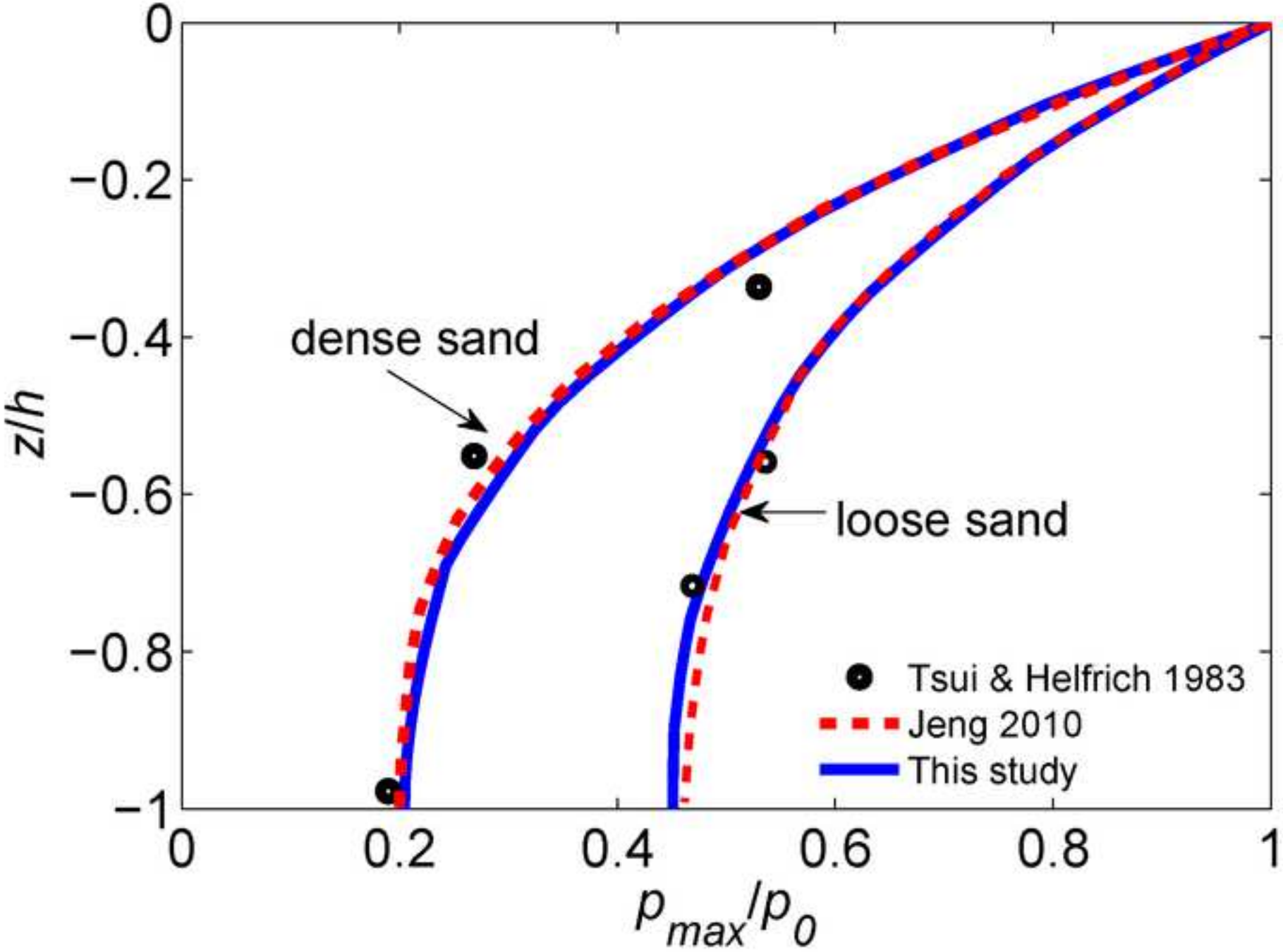

Figure 8
Click here to download high resolution image

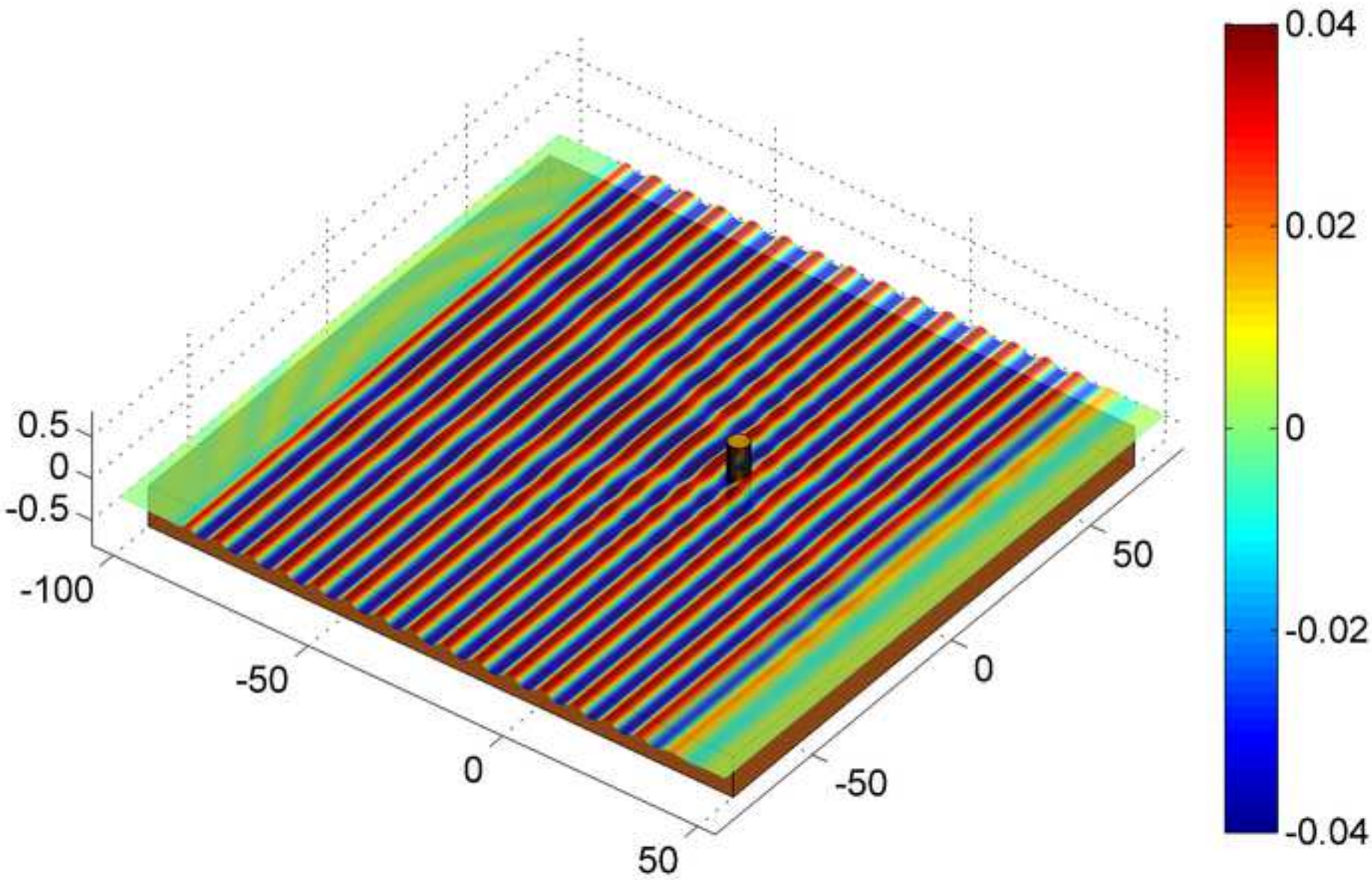

Figure 9
Click here to download high resolution image

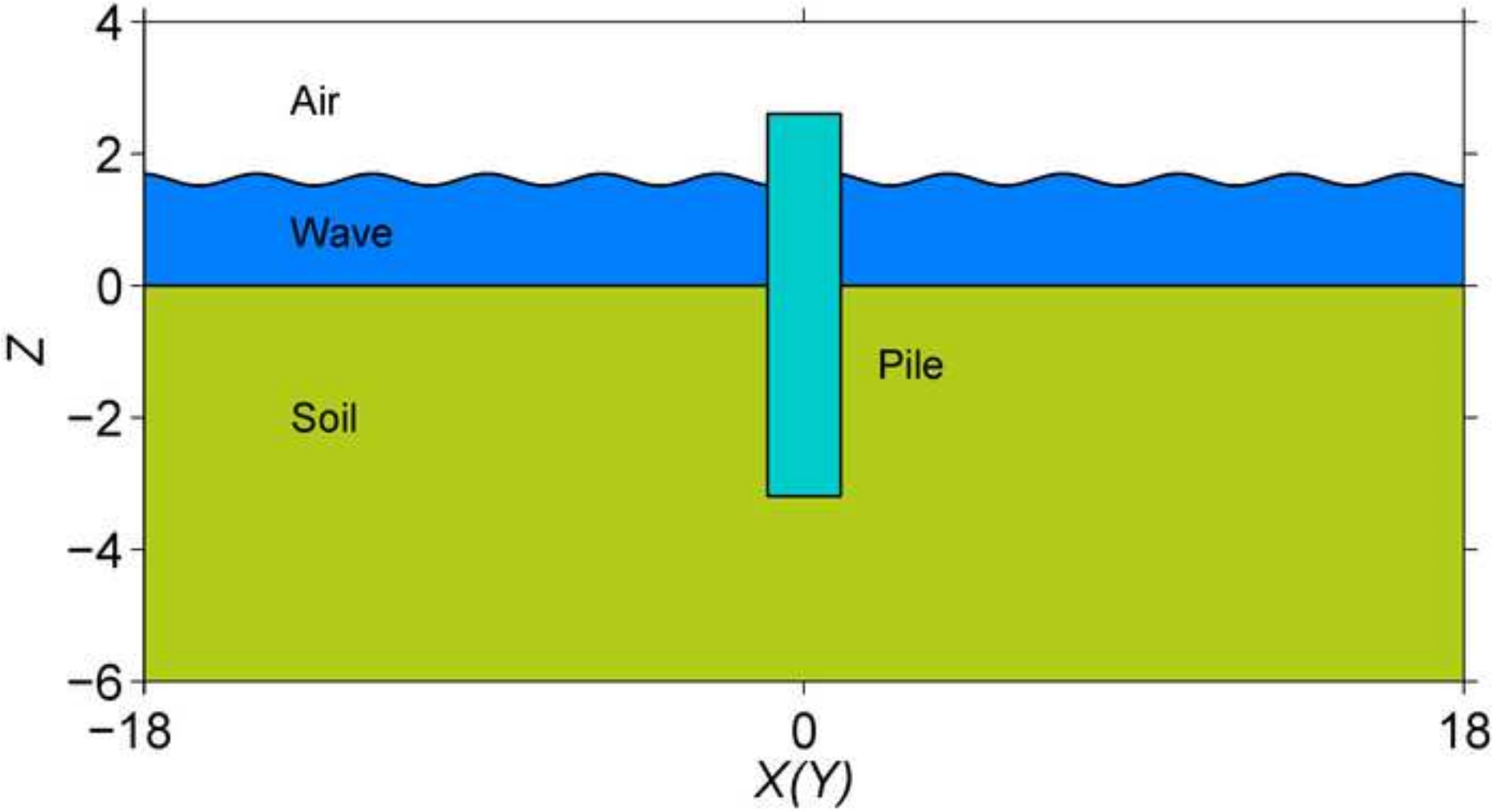

Figure 10
Click here to download high resolution image

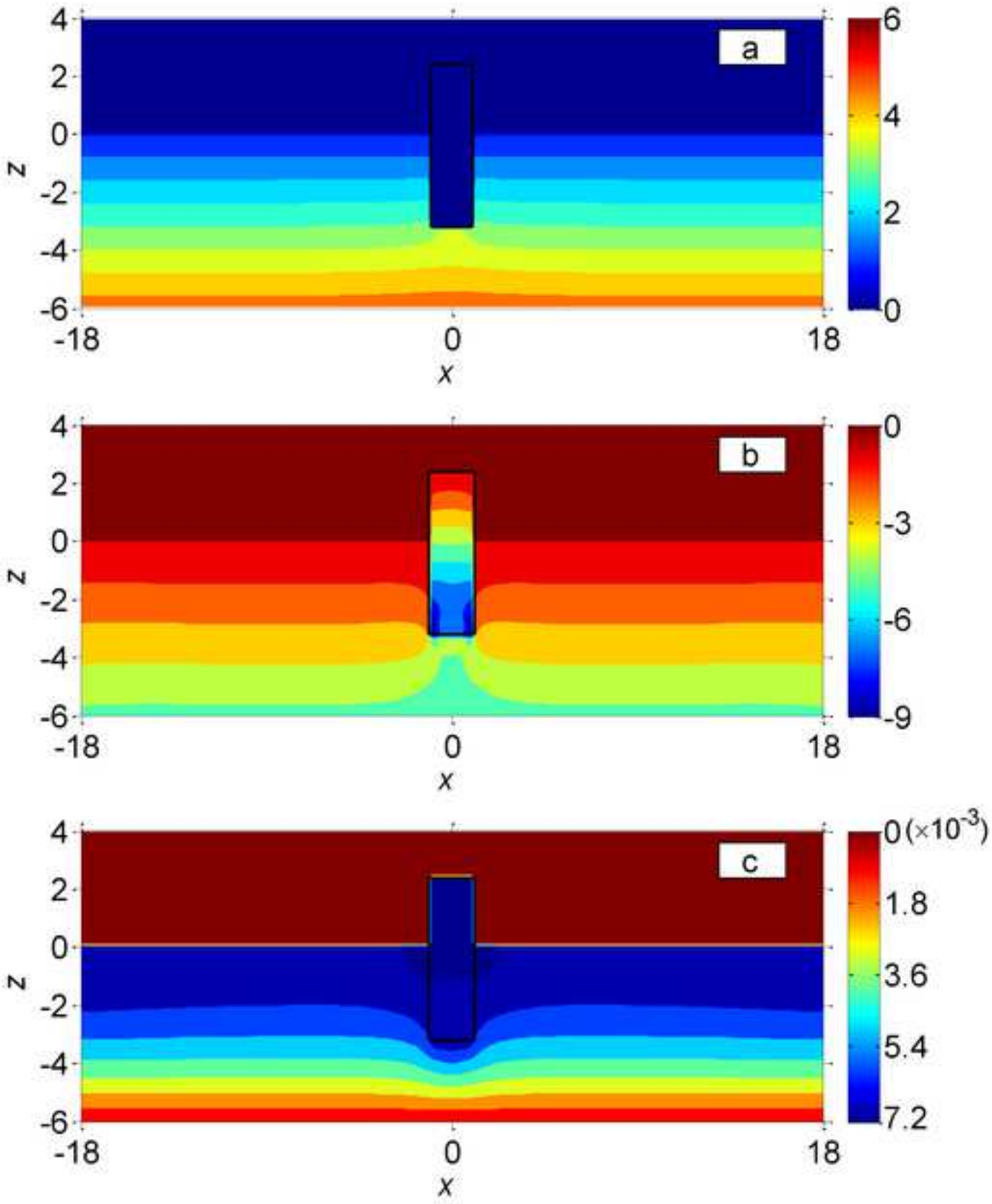

Figure 11
Click here to download high resolution image

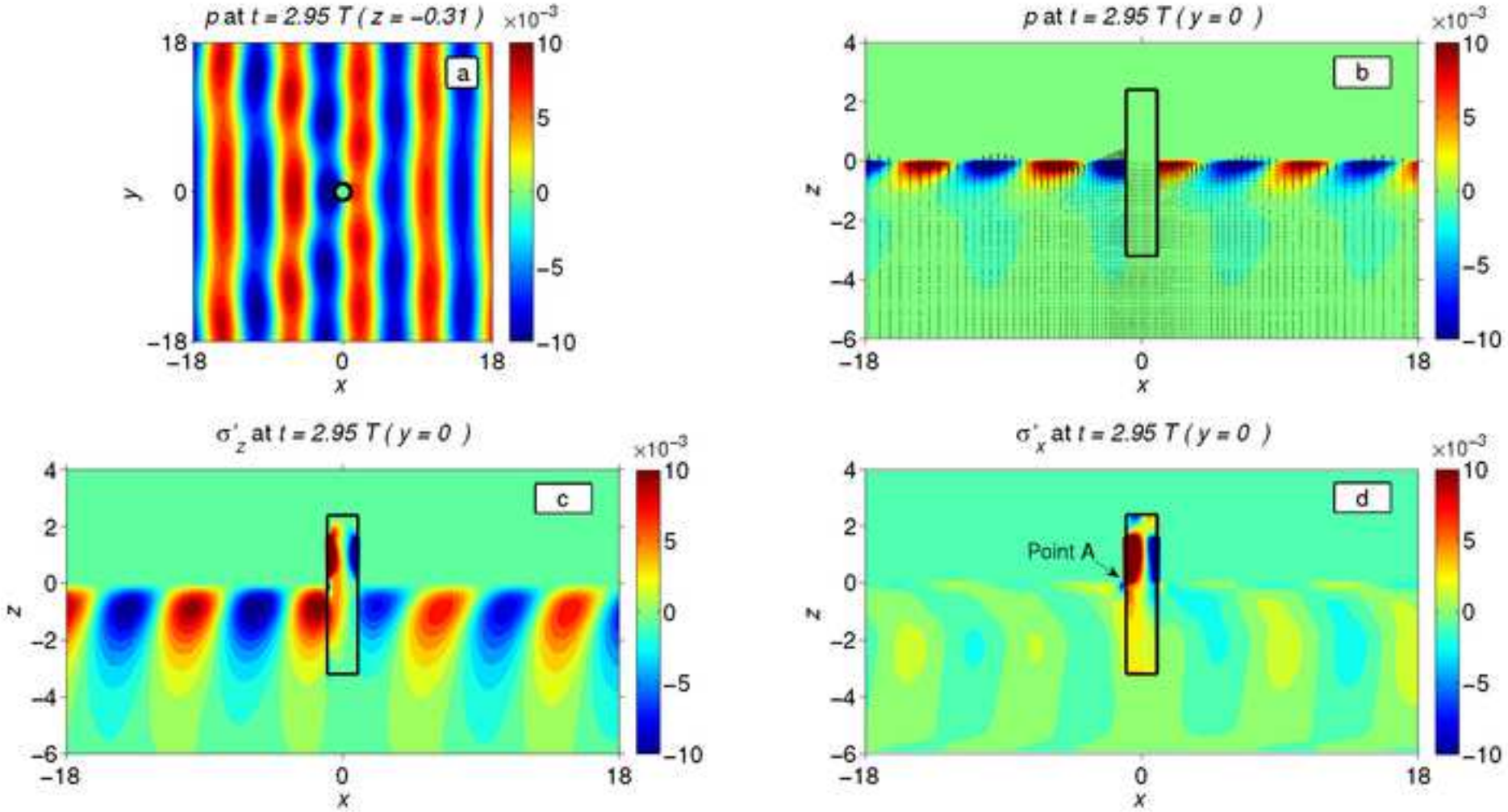

Figure 12
Click here to download high resolution image

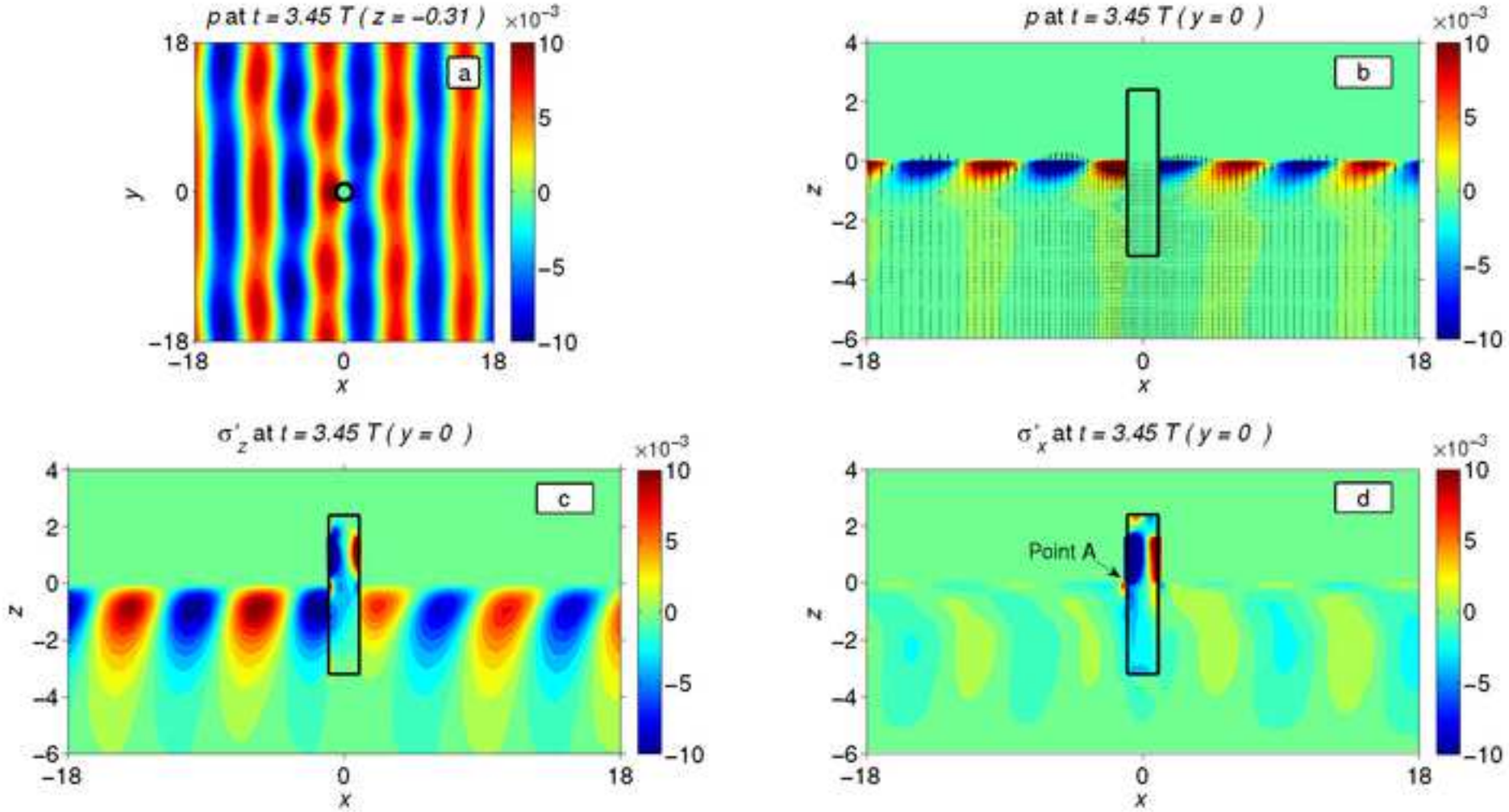

Figure 13
Click here to download high resolution image

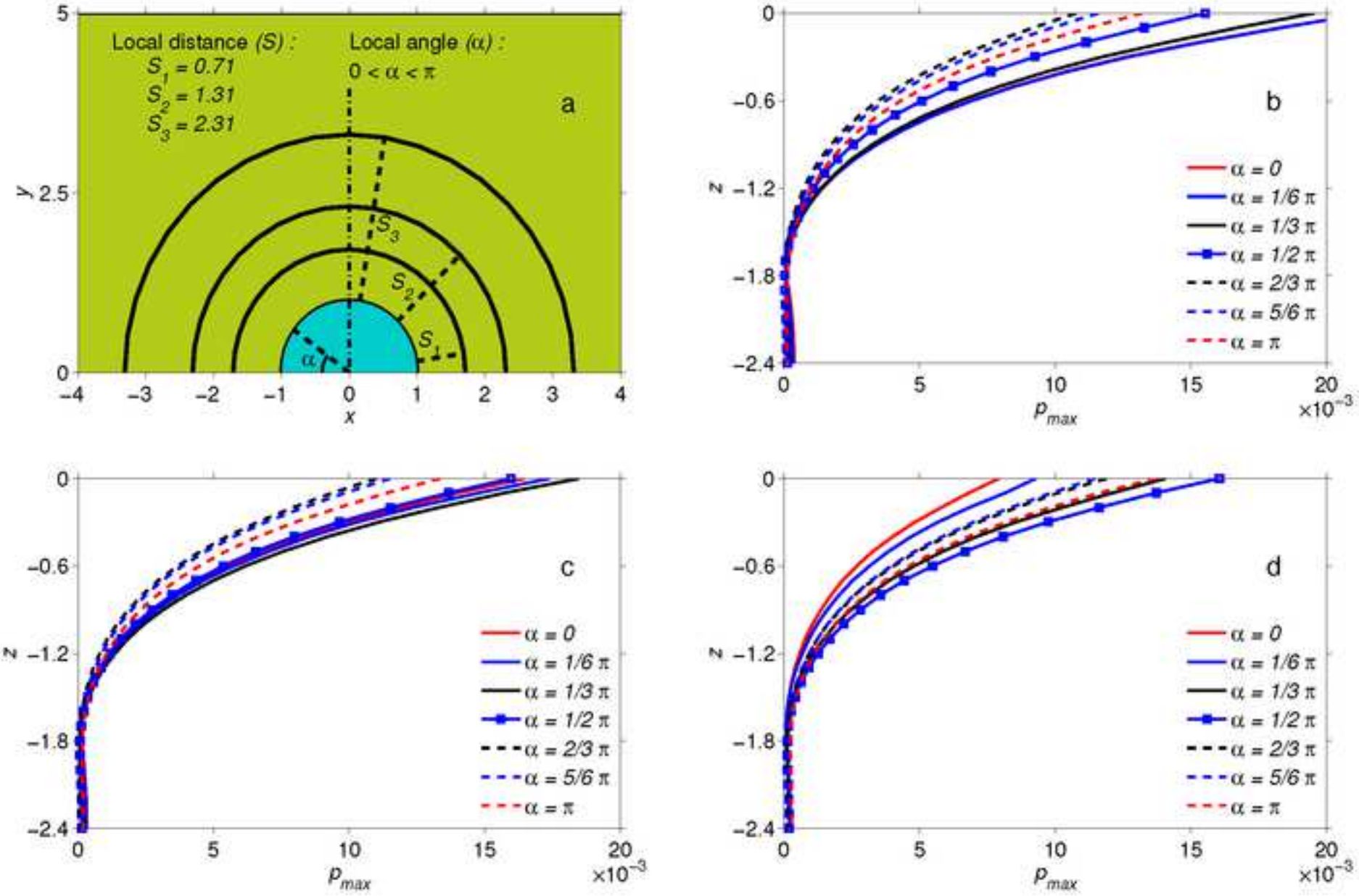

Figure 14
Click here to download high resolution image

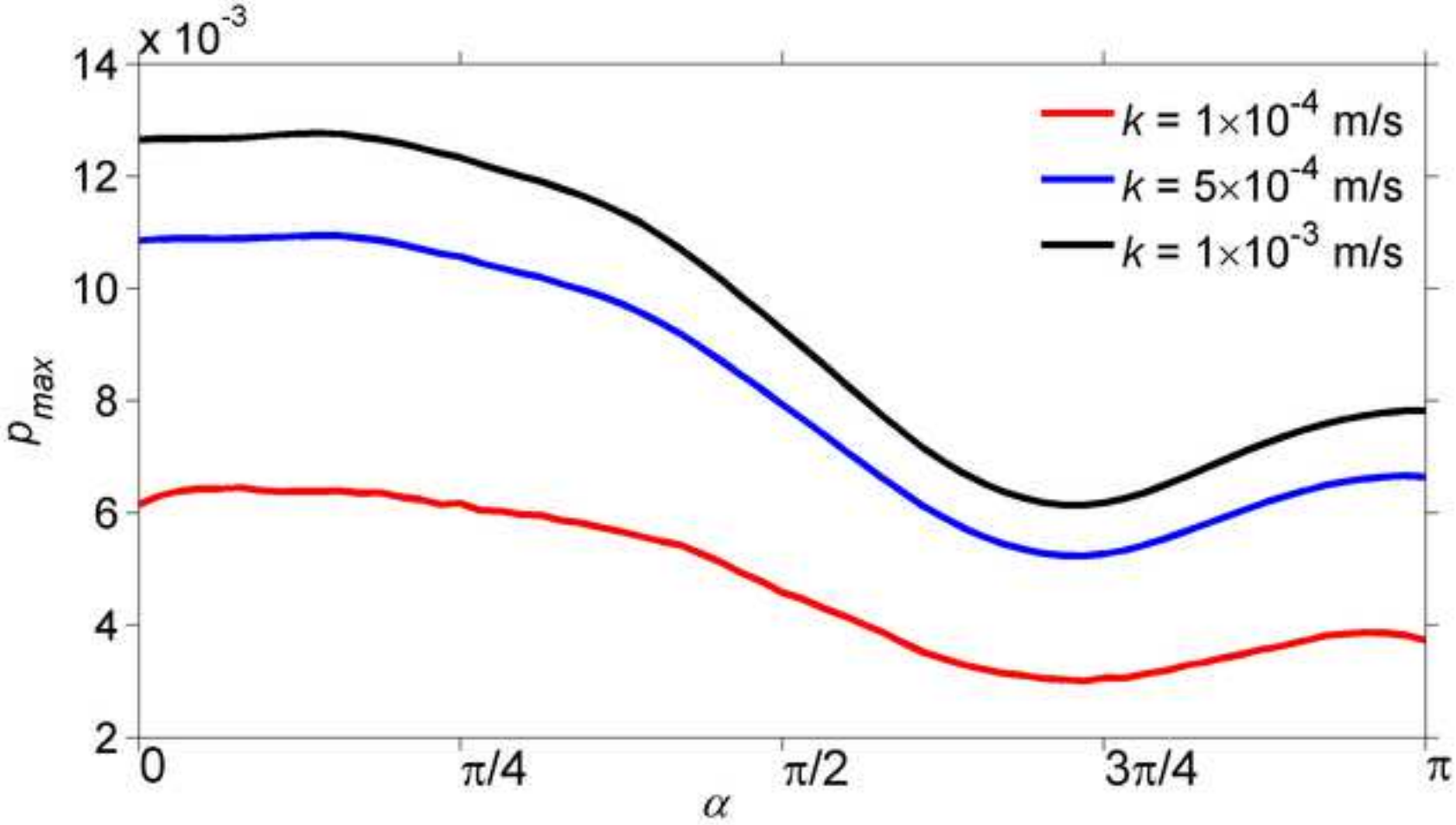

Figure 15
Click here to download high resolution image

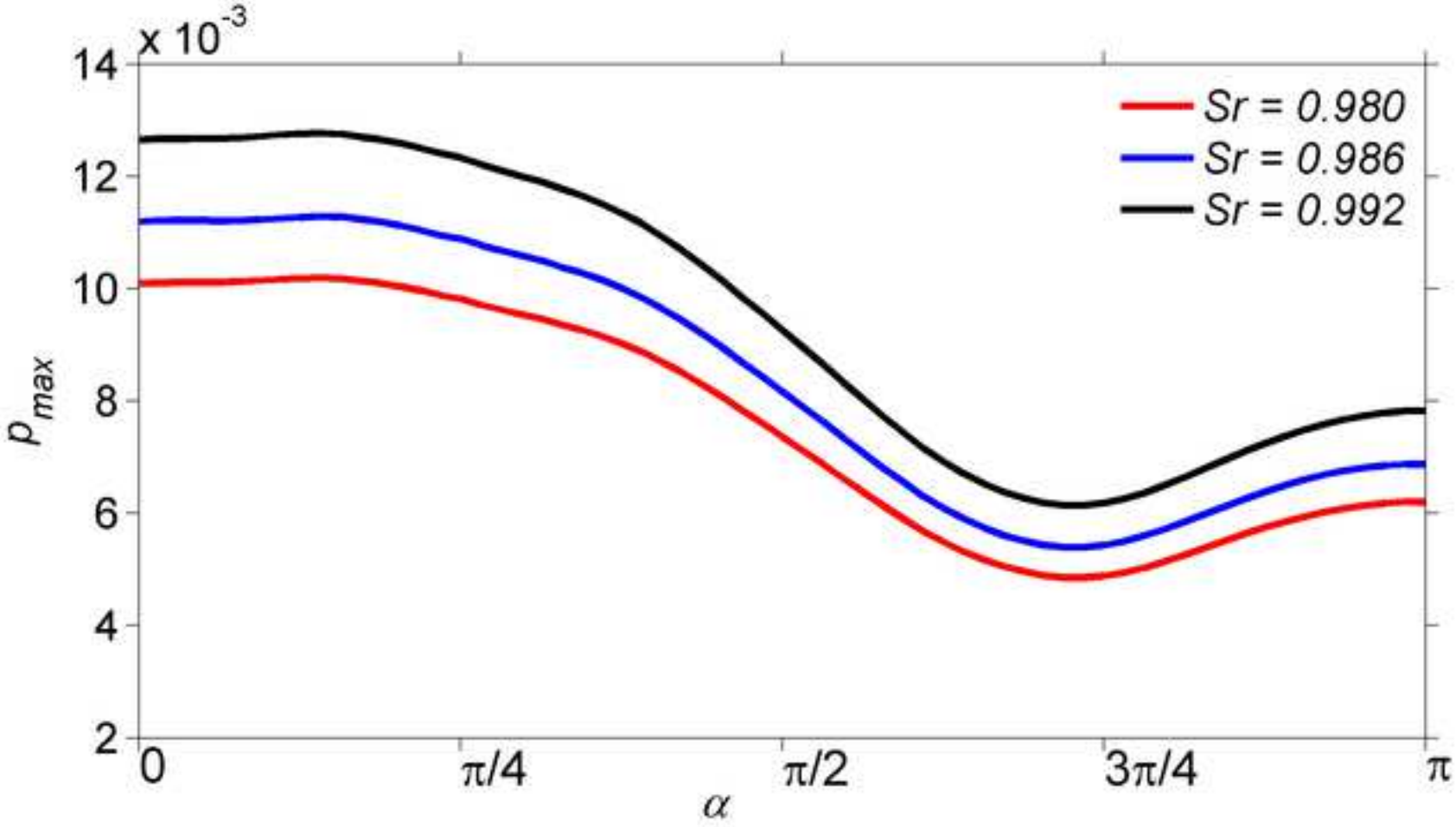

Figure 16
Click here to download high resolution image

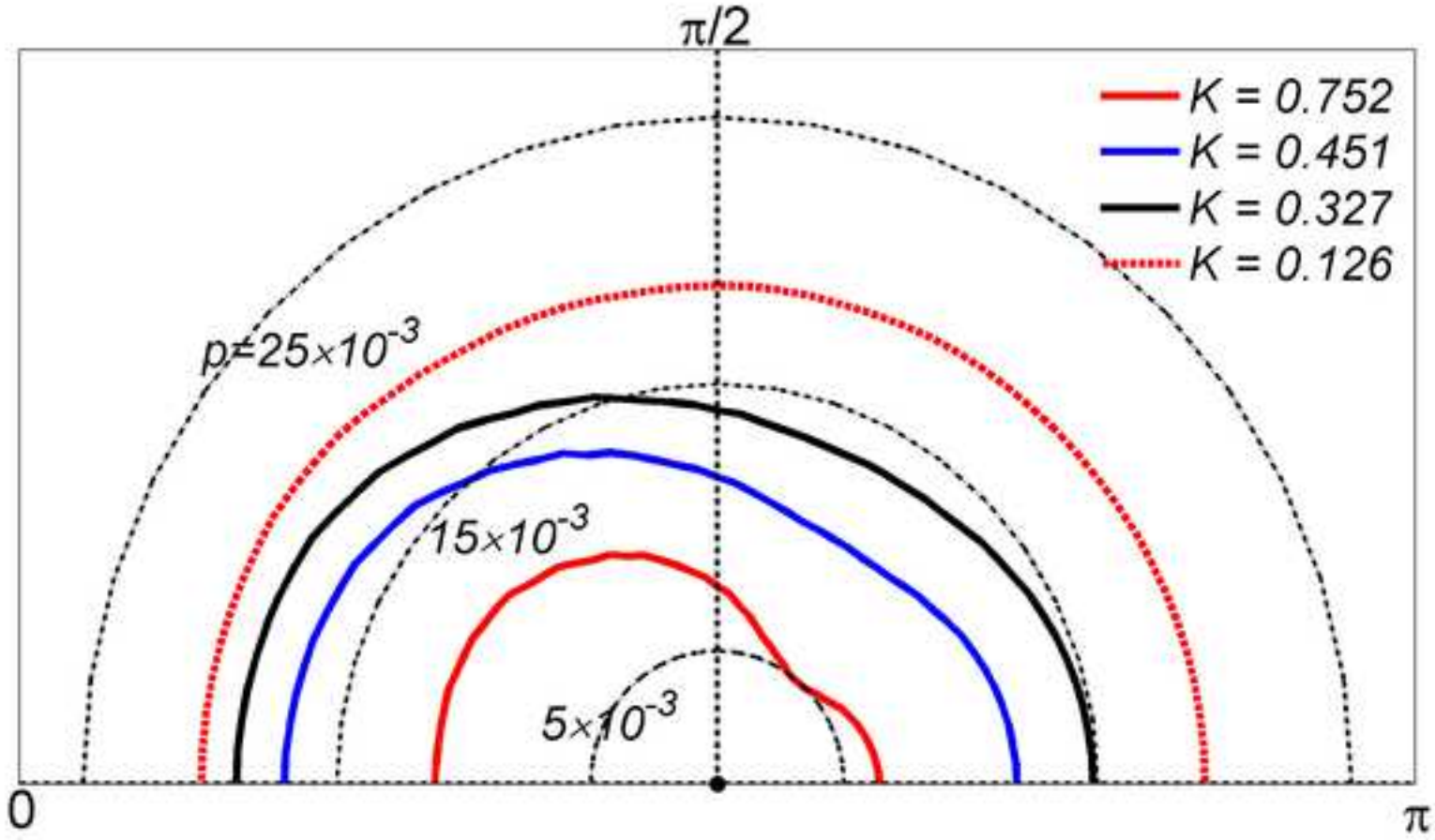

Figure 17
Click here to download high resolution image

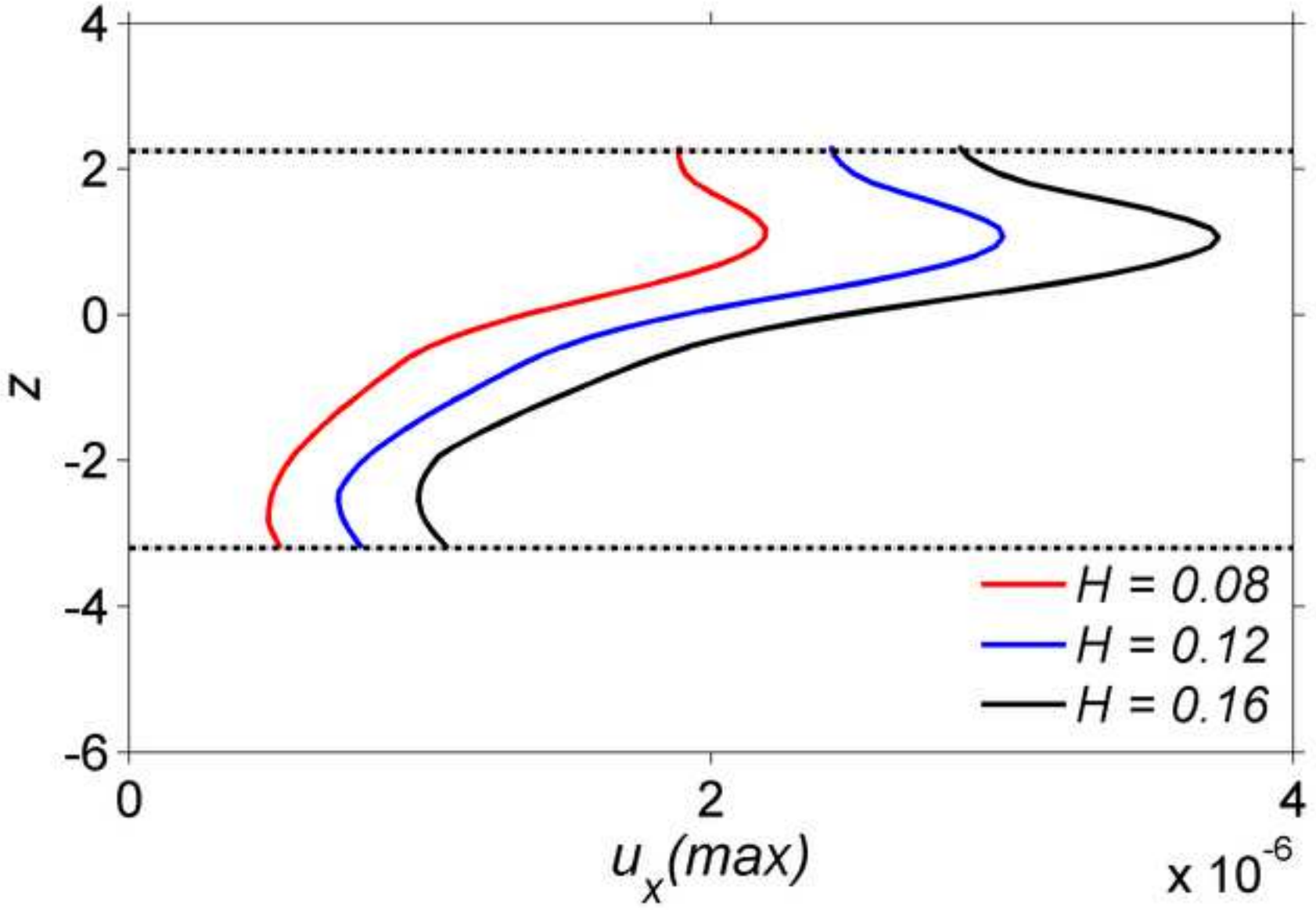

Figure 18
Click here to download high resolution image